Optimal placement of distributed optic fiber sensors with the modified Constitutive Relation Error

Jose Andres Perez Orozco, Ludovic Chamoin, Julien Cortial, Maya de Buhan, Bruno Soulier

Mechanical Systems and Signal Processing 238 (2025) 113206

Contents lists available at ScienceDirect

Mechanical Systems and Signal Processing

journal homepage: www.elsevier.com/locate/ymssp

Full length article

Optimal placement of distributed optic fiber sensors with the modified Constitutive Relation Error

José Andrés Pérez Orozco [a,b], Ludovic Chamoin [a,*], Julien Cortial [b], Maya de Buhan [b], Bruno Soulier [a]

[a] Université Paris-Saclay/CentraleSupélec/ENS Paris-Saclay/CNRS, LMPS - Laboratoire de Mécanique Paris-Saclay, 4 avenue des Sciences, Gif-sur-Yvette, 91190, Essonne, France

[b] Safran Tech, Digital Sciences and Technologies, Rue des Jeunes Bois, Magny-Les-Hameaux, 78114, Yvelines, France

ARTICLE INFO

Communicated by S. Laflamme

Keywords:
Fisher Information Matrix
Data assimilation
Optimal sensor placement
Optimization algorithms
Inverse problems
Modified Constitutive Relation Error
B-Splines representation

ABSTRACT

This paper presents a novel Optimal Sensor Placement strategy tailored to model updating problems based on the modified Constitutive Relation Error (mCRE) functional. It offers a credible alternative to classical functionals by optimizing structural parameters alongside mechanical fields, achieving the best trade-off between available measured data and physical knowledge without any additional *a priori* assumption. The proposed approach leverages the strong connection between mCRE and Bayesian inference to develop a new Fisher Information Matrix based on mCRE, incorporating the sensitivity of the mCRE mechanical fields to updated parameters. The mCRE-based optimization strategy leads to increased robustness with respect to measurement noise, deviation in the sensor placement, and modeling bias. While many of the developments in this work apply to various sensor types, additional constraints are included to focus on distributed optic fiber sensors (DOFS). The shape of the fiber is represented using B-Splines, making the control point coordinates the design variables. Constraints on maximum fiber length and minimum curvature radius are treated as penalty terms in the fitness function, optimized using a genetic algorithm. The proposed methodology is validated on isotropic and orthotropic elasticity using 2D and 3D geometries.

1. Introduction

Structural Health Monitoring (SHM) together with data assimilation is an increasingly used technique to evaluate the health of a structure through data acquired from on-board sensors [1,2]. This work focuses on a crucial factor in SHM, namely, optimized sensor placement [3–7], to ensure that the most informative data is collected. Most approaches for optimal sensor placement are quite similar and can usually be formulated as the selection of a subset of locations from a larger set of candidate locations. The key differences lie in the cost function and the optimization algorithm used [8].

Among the various cost functions used for sensor placement optimization, those based on the Fisher Information Matrix (FIM) [9,10] are the most commonly used. Typical sensor performance metrics include its trace (A-optimality) [11] and its determinant (D-optimality) [4,12]. A major contribution of this work is the development of a Fisher Information Matrix tailored to the modified Constitutive Relation Error (mCRE) framework. This new matrix, referred to as the modified FIM (mFIM), provides a rigorous and theoretically grounded tool to derive sensor performance metrics compatible with the mCRE. The mCRE is a method

* Corresponding author.
E-mail address: ludovic.chamoin@ens-paris-saclay.fr (L. Chamoin).

https://doi.org/10.1016/j.ymssp.2025.113206
Received 27 March 2025; Received in revised form 24 June 2025; Accepted 5 August 2025

used to solve inverse problems in structural mechanics. Compared to classical deterministic and stochastic approaches, the mCRE has demonstrated improved convexity properties [13,14] and greater robustness against noise and corrupted measurements [15–17]. Furthermore, it is a natural hybrid strategy that recovers the optimal state as a compromise between model outputs and experimental observations. However, optimal sensor placement metrics for the mCRE remain largely unexplored. Recently, only Diaz et al. [18] have introduced this topic in the context of low-frequency dynamics.

To demonstrate the capabilities of the proposed mFIM, we focus on distributed optical fiber sensors (DOFS), a particularly promising class of sensors for SHM. These sensors offer several benefits: they are lightweight, provide high spatial resolution, and allow for continuous strain measurements along the length of a single optical fiber. Their increasing use in aerospace, civil, and mechanical structures stems from the ability to deploy inexpensive telecom-grade fibers with minimal cabling and structural intrusion [19].

Unlike conventional discrete sensors, DOFS require a fundamentally different approach to placement. A single fiber contains all sensing points, meaning that one cannot optimize individual sensor locations independently. Instead, the fiber path must be optimized as a continuous geometric object, subject to physical constraints such as maximum length and allowable curvature.

Despite their advantages, there is little work on optimizing DOFS placement. Notably, the work of Li et al. [8] applies a genetic-based algorithm to provide an optimal sensor layout by maximizing the integration of a weighted functional of strain measures over the optic fiber length. The fiber is represented by a non-uniform rational B-spline (NURBS) curve, with design variables including specific control points and arc length coordinates of sensing elements. Additional constraints include the maximum allowed length and curvature, parameters that are commonly associated to optic fiber sensors. Other relevant works include Cazzulani et al. [3], which focuses on an optimal sensor layout for modal shapes reconstruction, and Ameduri et al. [20] which aims to maximize the probability of detection of damage induced by impact on a target structure. Both studies use genetic algorithms to perform the optimization, and the optic fiber's shape is described by interpolating key positions and orientations.

In the present study, we adopt a similar strategy by modeling the fiber path using B-spline curves and performing the optimization with a differential evolution algorithm, while enforcing physical constraints on the fiber's maximum curvature and total length. However, we extend this approach in a significant way by evaluating sensor performance using both the classical Fisher Information Matrix (FIM) and the newly developed modified FIM (mFIM), optimizing in each case the determinant (D-optimality criterion). Numerical experiments conducted on 2D and 3D mechanical structures demonstrate that the mFIM consistently outperforms the traditional FIM. This improvement stems from the properties of the mCRE functional, leading to a more robust sensor placement strategy. Specifically, the optimized placement shows greater resilience to measurement noise, practical misalignment of the fiber sensor relative to its nominal optimal path, and modeling bias.

The paper is organized as follows. Section 2 provides an introduction to inverse problems, detailing classical approaches to solve them stochastically, and their link to sensor performance metrics based on Fisher Information. Section 3 explains the modified Constitutive Relation Error (mCRE) concept, and Section 4 introduces a Fisher Information Matrix derived from the mCRE metric. Since the considered sensors are optic fibers, Section 5 details the considerations that are taken into account to parametrize the fiber's path. Afterwards, Section 6 introduces the cost function and the steps involved in during the optimization process. Finally, results for 2D and 3D linear isotropic and orthotropic elasticity cases are presented in Section 7.

2. Classical sensor performance metrics based on Fisher Information

2.1. Basics on inverse problems

In computational mechanics, inverse problems determine unknown input parameters $\theta \in \mathbb{R}^p, p \in \mathbb{N}$ from limited, noisy observations $X_{obs} \in \mathbb{R}^{N_S}$. However, these observations differ from model predictions due to measurement noise (ω_{obs}) or modeling errors (ω_{mod}) [18,21]:

$$X_{obs} = \Pi X(\theta_{real}) + \omega_{obs} + \omega_{mod} \tag{1}$$

where Π is an interpolation matrix to extract information at the sensor locations. Inverse problems can be solved deterministically or stochastically. The latter approach is preferred as it naturally accounts for parameter uncertainties. Bayesian inference provides a probabilistic framework for this objective:

$$\pi(\theta|X_{obs}) \propto \pi(X_{obs}|\theta)\pi_0(\theta) \tag{2}$$

where $\pi_0(\theta)$ is the prior distribution, $\pi(X_{obs}|\theta)$ is the likelihood distribution, and $\pi(\theta|X_{obs})$ is the updated or posterior probability density function on θ after taking observations into account (and the solution to the inverse problem). Considering Gaussian distributions, $\pi_0(\theta)$ and $\pi(X_{obs}|\theta)$ have the form:

$$\pi_0(\theta) \propto exp\left[-\frac{1}{2}(\theta-\theta_0)^T\Sigma_0^{-1}(\theta-\theta_0)\right] \tag{3}$$

$$\pi(X_{obs}|\theta) \propto exp\left[-\frac{1}{2}(X_{obs}-\Pi X(\theta))^T[\Sigma_{mod}+\Sigma_{obs}]^{-1}(X_{obs}-\Pi X(\theta))\right] \tag{4}$$

where θ_0 contains *a priori* parameter values, and Σ_0, Σ_{mod} and Σ_{obs} respectively denote the prior, model, and observation covariance matrices. In this framework, the solution of the inverse problem is a probability distribution, but several point indicators can be obtained from it. One is often interested in the maximum *a posteriori*, which is normally referred as the "identified" parameter θ_{opt}, and its variance. In instances where the objective is to identify multiple parameters ($\theta \in \mathbb{R}^p$ and $p > 1$), a covariance matrix is recovered to assess the degree of confidence in the parameter identification process.

2.2. Optimal sensor placement and Fisher Information

The goal of optimal sensor placement is to reduce the uncertainty in identified parameters by choosing sensor locations that maximize information gain. This uncertainty is commonly quantified via the Fisher Information Matrix (FIM), which measures the sensitivity of the likelihood function to changes in parameters. For unbiased estimators, the inverse of the FIM gives a lower bound on the parameter covariance matrix (Cramér–Rao bound) [9]. Thus, maximizing the FIM reduces parameter uncertainty. A common approach is to maximize the determinant of the FIM, known as D-optimality [3,4,10,12,22].

The FIM is defined as the covariance of the score, where the score is the gradient of the log-likelihood probability density function with respect to the parameter vector θ [9].

$$FIM = \mathbb{E}\left[\left(\frac{\partial \log \pi(X_{obs}|\theta)}{\partial \theta} \right)^T \left(\frac{\partial \log \pi(X_{obs}|\theta)}{\partial \theta} \right) \Bigg|_{\theta_{opt}} \right] \tag{5}$$

In this context, $\mathbb{E}$ denotes the mathematical expectation. Alternatively, if the analytical expression of second derivative of the log-likelihood is accessible, it yields [23]:

$$FIM = -\mathbb{E}\left[\frac{\partial^2 log\pi(X_{obs}|\theta)}{\partial \theta^2} \Bigg|_{\theta_{opt}} \right] \qquad \text{(see Annex A.1 for proof)} \tag{6}$$

It is then clear then that the Hessian of the log likelihood plays a key role in the in uncertainty quantification for parameter identification. However, this is not unique to the Bayesian approach. In deterministic settings such as Finite Element Model Updating (FEMU), parameter identification is often performed by minimizing a least-squares cost function. After convergence, the parameter covariance matrix is approximated as:

$$\Sigma_{\theta_{opt}} = \mathbb{H}^{-1}_{FEMU}$$

where $\mathbb{H}_{FEMU}$ is the Hessian of the cost function at θ_{opt}. This Hessian is equivalent to the FIM, allowing uncertainty propagation through the identification process [24].

For a Gaussian likelihood (see Eq. (4)), the FIM simplifies to:

$$FIM = \left(\Pi \frac{\partial X(\theta)}{\partial \theta} \right)^T \Sigma_\omega^{-1} \left(\Pi \frac{\partial X(\theta)}{\partial \theta} \right) \Bigg|_{\theta_{opt}} \tag{7}$$

Here, Σ_ω includes observation and modeling errors. Often, Σ_ω is approximated by the observation error covariance Σ_{obs}. This is usually done even if modeling errors might be present since they are not known *a priori* [24] (this shortcoming is addressed with our newly proposed modified FIM). In many applications, Σ_{obs} is diagonal (uncorrelated sensor noise) [11] and uniform across sensors, yielding the simplified FIM:

$$FIM = \frac{1}{\sigma^2_{obs}} \left(\Pi \frac{\partial X(\theta)}{\partial \theta} \right)^T \left(\Pi \frac{\partial X(\theta)}{\partial \theta} \right) \Bigg|_{\theta_{opt}} \tag{8}$$

This matrix depends on the sensor layout via Π, which selects measurement locations. Maximizing the determinant of the FIM improves parameter identifiability in all directions and enhances robustness to sensor perturbations or measurement noise.

A known limitation of FIM-based approaches is their dependence on θ, which is itself unknown. A practical workaround is to alternate between parameter identification and sensor optimization [25]. However, in practical applications, the sensor layout is often defined before the test. This is achieved either by using a reference or target parameter value, and should be optimal or near-optimal for any admissible parameter set.

3. The modified constitutive relation error

The previous developments are general for parameter identification and can be implemented in a variety of domains. In the following, the focus is placed on the specific context of structural mechanics. In this context, the forward problem determines the displacement field u typically approximated by a finite element solution u_h while the inverse problem estimates constitutive parameters θ. While other inverse problems exist, such as force reconstruction [26], this work focuses specifically on parameter identification. Among various inverse approaches, the modified Constitutive Relation Error (mCRE) stands out for its convexity properties [13,14] and robustness to noise [15–17]. Extending the Constitutive Relation Error (CRE) [27], the mCRE balances model confidence with experimental data U_{obs}, forming a hybrid framework for parameter identification. In the context of linear elasticity and following a discretization with the finite element method, the discretized CRE reads:

$$\mathcal{E}^{2^h}_{CRE}(\hat{U}, \hat{V}; \theta) = \frac{1}{2}(\hat{U} - \hat{V})^T \mathbb{K}(\hat{U} - \hat{V}) \tag{9}$$

where $(\hat{U}, \hat{V})$ represents a pair of kinematically and statically admissible solutions. The CRE (9) quantitatively reflects the confidence on modeling and is commonly referred in the literature to as the distance to model. Extending this, the mCRE [24,28] introduces a data-driven additional term referred to as the distance to data:

$$\mathcal{E}^{2^h}_{mCRE}(\hat{U}, \hat{V}; \theta) = \underbrace{\mathcal{E}^{2^h}_{CRE}(\hat{U}, \hat{V}; \theta)}_{\text{Distance to model}} + \underbrace{\frac{\alpha}{2} \left(\Pi \hat{U} - U_{obs} \right)^T \mathbb{G}_{obs} \left(\Pi \hat{U} - U_{obs} \right)}_{\text{Distance to data}} \tag{10}$$

where $\mathbb{G}_{obs}$ scales measurement errors, and α balances model fidelity against data fit. The optimal θ minimizes this functional:

$$\theta_{opt} = \underset{\theta}{\text{argmin}} \left[\min_{(\hat{U},\hat{V})} \quad \mathcal{E}^{2^h}_{mCRE}(\hat{U},\hat{V};\theta) \right] \tag{11}$$

This optimization problem is solved iteratively: first, $(\hat{U},\hat{V})$ are determined through the following saddle point conditions:

$$\begin{aligned} (\alpha(\Pi^T \mathbb{G}_{obs} \Pi) + \mathbb{K})\hat{U} &= \alpha(\Pi^T \mathbb{G}_{obs}) U_{obs} + F \\ \mathbb{K}\hat{V} &= F \\ \hat{V} &= \hat{U} + \Lambda \end{aligned} \tag{12}$$

where Λ is a Lagrange multiplier, and then θ is updated using convex minimization techniques [24]. It is emphasized that $\hat{U}$ is a hybrid quantity, based on the model and the experimental data.

3.1. Stochastic interpretation of the mCRE

To relate the mCRE and the Fisher Information matrix, a Bayesian interpretation of the mCRE is needed, which was developed by Deraemaeker and Ladevèze [29]. It is based on the combination of states of information proposed by Tarantola [21] and is equivalent to the Bayesian approach when the statistics of the measurement instrument are known. Within this framework, and considering Gaussian distributions, the mCRE-based likelihood probability density function reads:

$$\pi(U_{obs}|\theta) \propto exp\left[-\frac{1}{2} \left(\Pi\hat{U} - U_{obs} \right)^T \Sigma^{-1}_{obs} \left(\Pi\hat{U} - U_{obs} \right) \right] \times exp\left[-\frac{1}{2\alpha} (\hat{U} - \hat{V})^T \mathbb{K} (\hat{U} - \hat{V}) \right] \tag{13}$$

This distribution is visibly more complex than the one previously mentioned in (4). However, no assumption on the modeling error covariance (Σ_{mod}) must be made since the modeling error is already integrated in the distribution. When $\mathbb{G}_{obs} = \Sigma^{-1}_{obs}$ and considering a uniform prior defined in the interval $\theta \in [a, b]$, it yields:

$$\pi(\theta|U_{obs}) \propto \begin{cases} \pi(U_{obs}|\theta) \propto exp\left[-\frac{1}{\alpha} \mathcal{E}^2_{mCRE} \right] & \theta \in [a, b] \\ 0 \quad \theta \notin [a, b] \end{cases} \tag{14}$$

The interval of the prior can even be $\theta \in [-\infty, \infty]$. In this case, maximum *a posteriori* estimator of (14) equals the maximum *likelihood* estimator of (13) and corresponds to the minimizer of the deterministic cost function of the mCRE (11) [24].

3.2. Calibration of α

The mCRE is highly sensitive to the value of the scalar weight α. Limit values of α correspond to the classical least-squares minimization with no modeling error when $\alpha \to 0$, and to the pure CRE minimization with prescribed experimental data when $\alpha \to \infty$ [30]. An academic example is included in Annex A.3 to exemplify this behavior. Nguyen et al. [24] proposed that the value of α can be determined by leveraging the known noise levels in the measurements. The underlying idea is to ensure that the average squared distance between U_{obs} and $\hat{U}$ falls within the noise level.

$$\frac{1}{N_s} \mathbb{E}\left[\left(\Pi\hat{U} - U_{obs} \right)^T \Sigma^{-1}_{obs} \left(\Pi\hat{U} - U_{obs} \right) \right] \approx 1 \tag{15}$$

This is achieved by gradually decreasing the value of α until the condition described in (15) is satisfied. This approach is known as the Morozov criterion [31]. This has obvious physical sense, as reducing the distance even further would result in an overfitting of the noise. Fig. 1 exemplifies this process.

This can be reformulated though the following minimization problem:

$$\alpha_{opt} = \text{argmin}_{\alpha} \left| \frac{1}{N_s} \mathbb{E}\left[\left(\Pi\hat{U} - U_{obs} \right)^T \Sigma^{-1}_{obs} \left(\Pi\hat{U} - U_{obs} \right) \right] - 1 \right| \tag{16}$$

In the current work, this problem was solved using standard gradient-based optimization. The following choices were made:

- Initial value of α: Based on observed plateaus in the objective function, values beyond $\alpha > 1$ or $\alpha < 10^{-10}$ were avoided. An initial value of $\alpha = 10^{-4}$ was used.
- Stopping criterion: The optimization terminated when the discrepancy was within 1% of the target, i.e., when the absolute difference in (16) was less than 0.01.

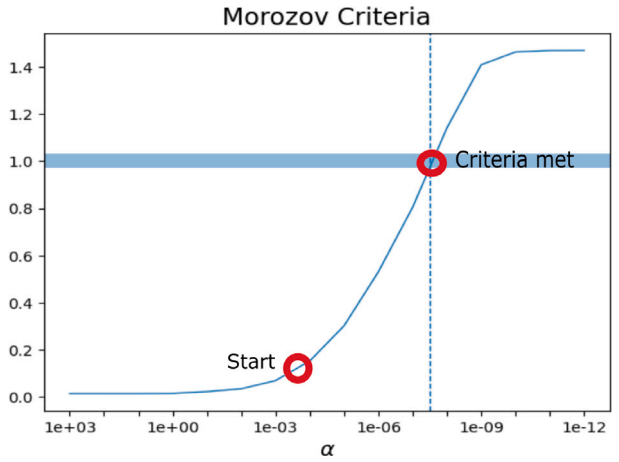

Fig. 1. Illustration of the strategy for the calibration of α.

4. FIM based on the mCRE

With the theory behind the mCRE established, attention can now be directed to its Fisher Information Matrix, referred to as the modified FIM (mFIM) to distinguish it from earlier developments. The concept of constructing a mFIM based on the mCRE was first introduced by Diaz et al. [18] in the context of low-frequency dynamics. This mCRE-based optimal sensor placement methodology was compared with classical techniques in terms of identification accuracy and validated through measurements from various scenarios and relative uncertainty assessments. The case of multiple damage scenarios was also addressed, demonstrating that although this approach introduces additional computational complexity, it results in more effective and robust sensor placement and improved model updating. This effectiveness persists even when the parameters to be identified undergo significant changes during experiments, such as evolving damage parameters over time. However, the formulation of the mFIM proposed in the previously mentioned work only considers the data misfit term of the mCRE functional, neglecting the contribution from the model discrepancy term. Specifically, the mFIM is defined as:

$$mFIM = \left(\Pi \frac{\partial \hat{U}}{\partial \theta} \right)^T (\Sigma_{obs})^{-1} \left(\Pi \frac{\partial \hat{U}}{\partial \theta} \right) \Bigg|_{\theta_{opt}} \tag{17}$$

In contrast, the modified Constitutive Relation Error (mCRE) consists of two terms, the distance to data and the distance to the model (10), both of which depend on sensor placement. Moreover, the relative importance of these terms is controlled by the parameter α, meaning one term may dominate the other depending on its value (as shown in Annex A.3).

A major contribution of this work lies in the development of a comprehensive theoretical framework for a modified Fisher Information Matrix that incorporates the full mCRE functional. By accounting simultaneously for both the data fidelity and model consistency terms, the proposed formulation provides a more rigorous and informative foundation for sensor placement strategies in structural mechanics, particularly in scenarios where a trade-off between measurement precision and model reliability must be carefully balanced.

To this end, the complete likelihood probability density function of the mCRE (13) is adopted. However, using the classical FIM formulation (5) poses a computational challenge: its expectation involves third and fourth moments (skewness and kurtosis), which are difficult to evaluate. This complexity becomes particularly problematic when maximizing the determinant of the modified FIM using a stochastic optimization algorithm like differential evolution, as it requires numerous matrix computations. To overcome this, the second derivative formulation of the FIM (6) is employed, leading to:

$$mFIM = \frac{1}{\alpha} \mathbb{E} \left[\frac{\partial^2 \mathcal{E}^{2h}_{mCRE}}{\partial \theta^2} \Bigg|_{\theta_{opt}} \right] \tag{18}$$

This expression is directly related to the Hessian of the mCRE:

$$\frac{\partial^2 \mathcal{E}^{2h}_{mCRE}}{\partial \theta^2} = \frac{1}{2} (\hat{U} - \hat{V})^T \frac{\partial^2 \mathbb{K}}{\partial \theta^2} (\hat{U} + \hat{V})^T + \hat{U}^T \frac{\partial \mathbb{K}}{\partial \theta} \frac{\partial \hat{U}}{\partial \theta} - \hat{V}^T \frac{\partial \mathbb{K}}{\partial \theta} \frac{\partial \hat{V}}{\partial \theta} \tag{19}$$

The intuition behind this relationship is straightforward and is illustrated for a single parameter in Fig. 2. Essentially, a sensor configuration that produces a higher curvature in the mCRE, analogous to a higher curvature in the posterior distribution, leads to a lower variance in the identified parameters.

While not directly linked to the Fisher Information Matrix, the Hessian of the mCRE has been previously employed as an indicator of the uncertainties in the parameter identification process. Charbonnel et al. [16] introduced the concept of confidence

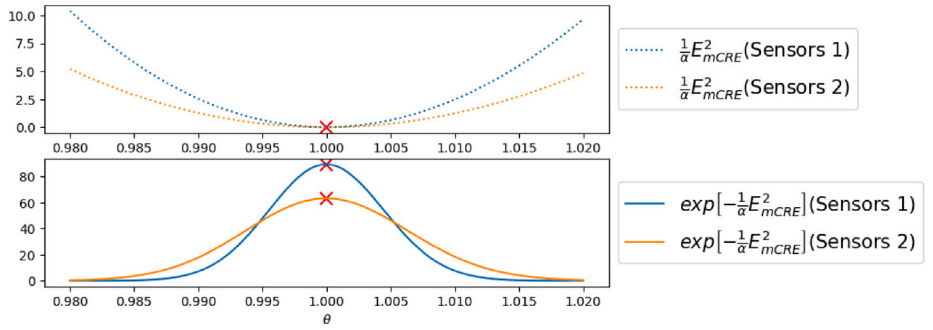

Fig. 2. Hessian of mCRE and variance of posterior distribution.

intervals within the deterministic mCRE framework, proposing the use of a second-order Taylor expansion to approximate the mCRE functional. By analyzing how perturbations in the mCRE value influence the estimated parameters, this approach leverages the Hessian, as the shape of the second-order expansion at convergence is determined by it.

To calculate the expectation of (19), a procedure similar to that proposed by Deraemaeker and Ladevèze in [29] for evaluating the expectation of the mCRE is followed. To simplify the developments, the first expression in (12) is rewritten as:

$$\begin{aligned}(\alpha(\Pi^T\mathbb{G}_{obs}\Pi)+\mathbb{K})\hat{U} &= \alpha(\Pi^T\mathbb{G}_{obs})U_{obs}+F\\ &\downarrow\\ \mathbb{C}\hat{U} &= \mathbb{P}U_{obs}+F\end{aligned} \tag{20}$$

The observed quantities at each sensing location can be modeled independently, assuming the measurement noise is uncorrelated, with variance σ^2 and zero mean, as follows:

$$\begin{aligned}U_{obs_i} &= U^0_{obs_i}+\delta U_{obs_i}\\ \mathbb{E}[\delta U_{obs_i}] &= 0\\ \mathbb{E}[\delta U_{obs_i}\delta U_{obs_j}] &= \sigma^2\delta_{ij}\end{aligned} \tag{21}$$

Here, the zero superscript refers to the constant portion (as in $U^0_{obs_i}$), and the delta symbol refers to the random portion (as in δU_{obs_i}). Thus, U_{obs} can be separated into the sum of its constant and random components as:

$$U_{obs} = \underbrace{\sum_{i=1}^{N_S} U^0_{obs_i} m_i}_{U^0_{obs}} + \underbrace{\sum_{i=1}^{N_S} \delta U_{obs_i} m_i}_{\delta U_{obs}} \tag{22}$$

where m is a unit vector basis, such that m_i equals 1 at measurement i and zero elsewhere; this basis contains N_S (number of sensors) vectors. A new basis ϕ is then introduced such that:

$$\mathbb{C}\phi_i = \mathbb{P}m_i \tag{23}$$

$\hat{U}$ can now also be written as a sum of constant and random portions:

$$\hat{U} = \underbrace{\sum_{i=1}^{N_S} U^0_{obs_i}\phi_i + \mathbb{C}^{-1}F}_{\hat{U}^0} + \underbrace{\sum_{i=1}^{N_S} \delta U_{obs_i}\phi_i}_{\delta U} \tag{24}$$

A similar procedure can be followed for $\frac{\partial\hat{U}}{\partial\theta}$. Following the approach in (23), a basis ψ is introduced such that:

$$-\mathbb{C}\psi = \frac{\partial\mathbb{K}}{\partial\theta}\phi \tag{25}$$

which allows $\frac{\partial\hat{U}}{\partial\theta}$ to be written as:

$$\frac{\partial\hat{U}}{\partial\theta} = \underbrace{\sum_{i=1}^{N_S} U^0_{obs_i}\psi_i}_{\frac{\partial\hat{U}^0}{\partial\theta}} + \underbrace{\sum_{i=1}^{N_S} \delta U_{obs_i}\psi_i}_{\delta\frac{\partial\hat{U}}{\partial\theta}} \tag{26}$$

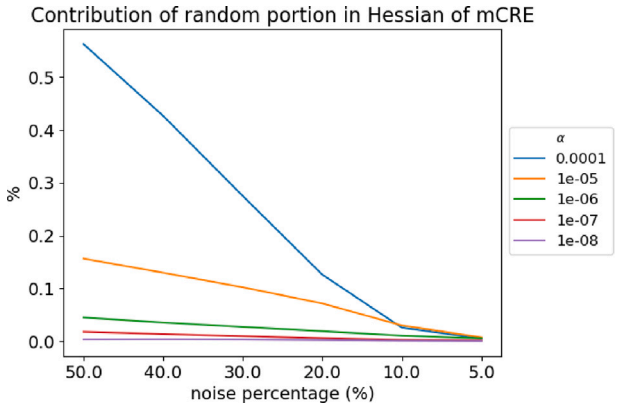

Fig. 3. Contribution of random terms in the Hessian of mCRE.

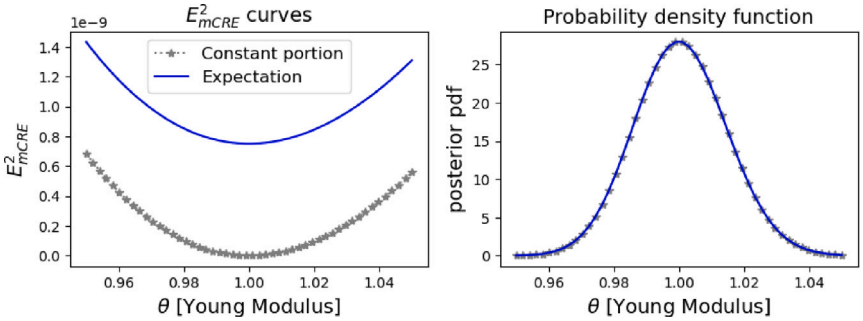

Fig. 4. Expectation of mCRE.

With (24) and (26) in mind, the expectation of the Hessian of the mCRE can be calculated. However, the constant and random portions must first be identified:

$$\frac{\partial^2 \mathcal{E}^{2^h}_{mCRE}}{\partial\theta^2} = \frac{1}{2}(\hat{U}^0 - \hat{V} + \delta\hat{U})^T \frac{\partial^2 \mathbb{K}}{\partial\theta^2}(\hat{U}^0 + \hat{V} + \delta\hat{U})^T + (\hat{U}^0 + \delta\hat{U})^T \frac{\partial \mathbb{K}}{\partial\theta}\left(\frac{\partial \hat{U}^0}{\partial\theta} + \delta\frac{\partial\hat{U}}{\partial\theta}\right) - \hat{V}^T \frac{\partial\mathbb{K}}{\partial\theta}\frac{\partial\hat{V}}{\partial\theta} \tag{27}$$

Considering that the expectation of a constant is the value of the constant, the expectation of the Hessian is finally:

$$\mathbb{E}\left[\frac{\partial^2 \mathcal{E}^{2^h}_{mCRE}}{\partial\theta^2}\right] = \mathbb{E}\left[\frac{1}{2}\delta\hat{U}^T \frac{\partial^2\mathbb{K}}{\partial\theta^2}\delta\hat{U}^T + \delta\hat{U}^T\frac{\partial\mathbb{K}}{\partial\theta}\delta\frac{\partial\hat{U}}{\partial\theta}\right] + \hat{U}^{0^T}\frac{\partial\mathbb{K}}{\partial\theta}\frac{\partial\hat{U}^0}{\partial\theta} - \hat{V}^T\frac{\partial\mathbb{K}}{\partial\theta}\frac{\partial\hat{V}}{\partial\theta} \tag{28}$$

where:

$$\begin{cases} \mathbb{E}\left[\frac{1}{2}\delta\hat{U}^T\frac{\partial^2\mathbb{K}}{\partial\theta^2}\delta\hat{U}^T\right] &= \sum_{i=1}^{N_S}\sum_{j=1}^{N_S}\phi_i^T\frac{\partial^2\mathbb{K}}{\partial\theta^2}\phi_j\mathbb{E}[\delta U_{obs_i}\delta U_{obs_j}] \\ \mathbb{E}\left[\delta\hat{U}^T\frac{\partial\mathbb{K}}{\partial\theta}\delta\frac{\partial\hat{U}}{\partial\theta}\right] &= \sum_{i=1}^{N_S}\sum_{j=1}^{N_S}\phi_i^T\frac{\partial\mathbb{K}}{\partial\theta}\psi_j\mathbb{E}[\delta U_{obs_i}\delta U_{obs_j}] \end{cases} \tag{29}$$

It is noted that to compute the expectation of the Hessian, only the observation error variance is required ($\mathbb{E}[\delta U_{obs_i}\delta U_{obs_j}] = \sigma^2\delta_{ij}$).

Similar to the mCRE functional itself, the expectation of its Hessian is dependent on parameter α. The random portions increase as α and the noise percentage increase. However, for the constitutive laws analyzed and noise levels up to 40%, it was observed that the expected value of the random component of the Hessian remained approximately four orders of magnitude smaller than the deterministic part, contributing less than 1% to the total expected value of the Hessian. As seen in Fig. 3, this observation holds for a wide range of α values, including those larger than the ones used throughout this work, which lie in the range $[10^{-9}, 10^{-5}]$.

This is exemplified in Fig. 4, which shows the curves for the following inverse problem: identifying a theoretical Young modulus of 1 [Pa] in an isotropic homogeneous plate subjected to tension (similar to the case study that will be presented in Section 7.1). Fig. 4 compares the complete expectation of the mCRE (blue), and the constant portion alone (gray). The complete expectation has an offset from zero, reflecting the fact that no value of the Young modulus results in zero error when the measurements contain noise. However, the overall shape of the mCRE curve and the posterior distribution remain nearly unchanged. For this reason, the sensor placement optimization process in the remainder of this work focuses on the constant portion of the Hessian. When only the

constant portion is needed, the mFIM (18) simplifies to:

$$mFIM = \frac{1}{\alpha}\left(\hat{U}^{0^T} \frac{\partial \mathbb{K}}{\partial \theta} \frac{\partial \hat{U}^0}{\partial \theta} - \hat{V}^T \frac{\partial \mathbb{K}}{\partial \theta} \frac{\partial \hat{V}}{\partial \theta} \Big|_{\theta_{opt}} \right) \tag{30}$$

In the case of a single parameter, maximizing the mFIM (30), and consequently the Hessian at θ_{opt}, increases the curvature of the probability density function (13) around this parameter value, leading to a lower variance. When multiple parameters are considered, a similar objective is achieved by maximizing the determinant of the FIM, ensuring that all principal directions contain high information content. It is important to note that this sensor placement optimization is often carried out without prior knowledge of the true parameter value; therefore, a reference value can be used to obtain an optimal or quasi-optimal solution.

Parallels can be drawn between the modified Fisher Information Matrix (mFIM) (30) and the original Fisher Information Matrix (FIM) (7), as both quantify sensitivity with respect to θ. However, while traditional methods rely on local evaluations at sensor positions using the projection matrix Π, the mFIM instead evaluates global quantities by incorporating the complete fields $\hat{U}$ and $\hat{V}$ along with their sensitivities to θ. This distinction is directly tied to the nature of the mCRE admissible fields, which are constructed based on observed data. Notably, even though only the constant portion of the mCRE was used, the influence of noise persists through $\mathbb{G}_{obs}$.

5. Representation of the optic fiber path

Sections 2 and 4 introduced general sensor performance metrics, but additional considerations are needed for optic fiber sensors. This section presents a B-Spline-based parametrization of the fiber path, enabling efficient placement optimization for fibers affixed to the surface of a structure. The approach can also be extended to embedded configurations, provided a target surface is defined, such as in laminated composite materials. It supports both flat and curved surfaces: in the flat case, fibers are defined directly in a 2D plane, while for curved geometries, the fiber path is defined on a surface described by a finite element mesh, allowing it to follow the structure geometry.

5.1. Parametrized shape of the fiber using B-Splines in a flat surface

Optic fiber sensors measure strain along their longitudinal direction at N_S positions, and while optimizing the coordinates and orientations of each sensing point is possible, it becomes impractical when N_S reaches hundreds or thousands, especially in Rayleigh Backscattering fibers, which provide near-continuous data [32].

To address this, the goal is to parametrize the fiber shape with $N \ll N_S$ parameters using B-Splines. While B-Splines were previously used for fiber placement [8], they were paired with simpler sensor performance metrics than those based on the FIM. Other approaches include the optimization of the position and tangent values of key points along the fiber [3,20].

Mathematically, a B-spline is a combination of Bezier curves, which results in a barycentric combination of N control points. The analytical expression is presented in (31), where the resulting curve $B(t)$ is a sum of polynomials (or basis functions) multiplied by the control polygon coordinates. An example of a B-Spline curve and its basis polynomial functions is shown in Fig. 5.

$$\begin{aligned} B(t) &= \sum_{i=0}^{i=N} CP_i M_i(t) \quad t \in [t_0, t_f] \\ \mathrm{CP} &= [CP_0, \ldots, CP_N] \quad \text{(Control polygon coordinates)} \\ \mathrm{M} &= [M_0(t), \ldots, M_N(t)] \quad \text{(Basis functions)} \end{aligned} \tag{31}$$

Control points can be selected from discrete locations or defined continuously via their (X,Y,Z) coordinates.

5.2. Extension to curved 3D geometries

Most existing methods for sensor placement are limited to flat surfaces, restricting optical fiber placement to simple shapes. This work presents a method for placing fibers on smooth, curved 3D surfaces, acknowledging that optical fibers cannot bend sharply. The main innovation lies in generating a parametrized fiber path on a discretized curved surface (mesh). The process starts by identifying the region of interest, followed by selecting potential control points, either randomly (e.g., Latin Hypercube Sampling) or from surface mesh nodes.

For each configuration tested during optimization, a subset of control points defines a B-Spline path. Since the B-Spline may not lie on the mesh, it is projected orthogonally onto the surface. This projection can introduce non-smoothness, causing numerical issues when computing tangent vectors, critical as the fiber only senses along its axis. To address this, average filtering is applied.

This methodology is illustrated in Fig. 6, using a cylinder as reference geometry for illustration purposes.

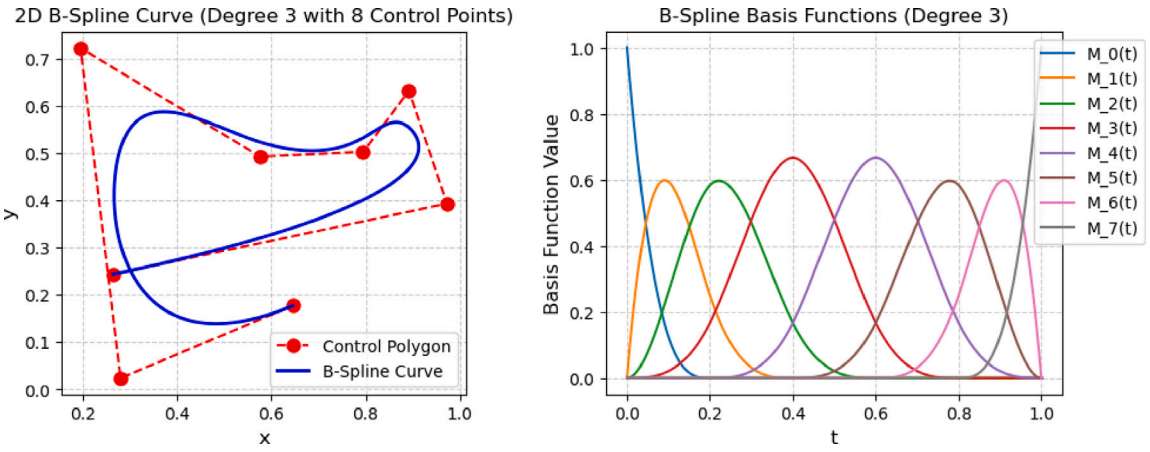

Fig. 5. An example of a B-Spline curve and its underlying basis.

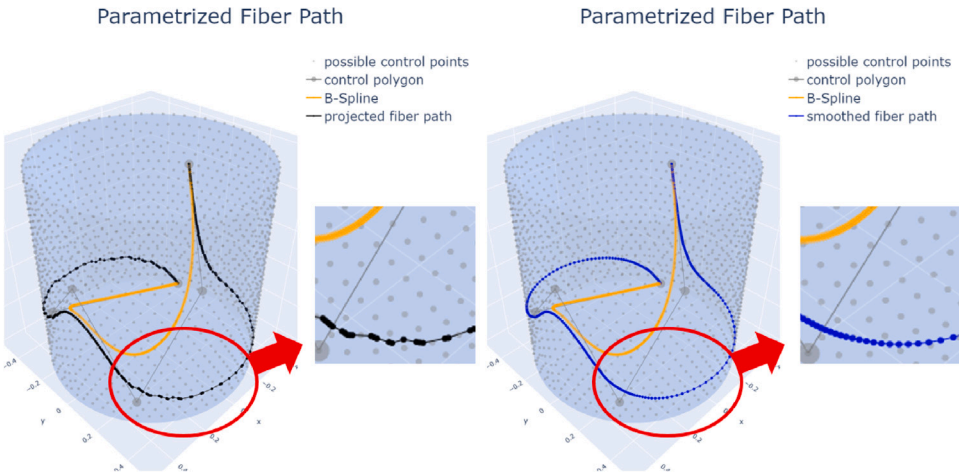

Fig. 6. Parametrized fiber path along a curved surface, results before and after filtering.

6. Optimization problem

6.1. Cost function

The procedure for optimizing the shape of the optic fiber using B-Splines, with the determinant of the Fisher Information matrix as the sensor performance metric, is now presented. Three matrices are considered:

- The classical FIM (8)
- The one proposed by Diaz et al. [18], referred as mFIM1 (17)
- Our newly proposed matrix, referred as mFIM2 (30)

Considering that CP is a vector containing the control polygon coordinates, the optimization problem thus reads:

$$\begin{aligned} CP_{opt} &= \underset{CP}{\operatorname{argmin}} -det(\mathrm{M}) \quad M \in [FIM, mFIM1, mFIM2] \\ &s.t. \\ &\text{Fiber length constraint: } L \leq L_{Lim} \\ &\text{Curvature radius constraint: } C \geq C_{Lim} \end{aligned} \tag{32}$$

To solve (32) using a differential evolution algorithm, the following cost (or fitness) function is introduced:

$$f = -det(\mathrm{M}) \times k^{-max\left(\frac{L}{L_{lim}}, 1\right)+1} \times k^{-max\left(\frac{C_{lim}}{C}, 1\right)+1} \tag{33}$$

Table 1
Impact of penalization constant (targets: 0.15 m [max length] and 0.01 m [min radius]).

Penalization constant	Length obtained [m]	Minimum radius obtained [m]
2	0.20073	0.01018
3	0.15554	0.01020
4	0.15076	0.01040
5	0.15007	0.01045

where k is a constant that determines the severity of the penalization.

6.1.1. Maximum length of the fiber

One of the main challenges associated with optic fibers is their integration within the structure. For instance, when embedding an optic fiber in a carbon fiber composite, the diameter of the sensor is an order of magnitude larger than the structural fibers. As a result, it is likely that its presence will weaken the material due to the creation of resin pockets in its surroundings, which might act as a crack initiator. However, several experiments show negligible impact when implemented properly [32]. Still, an overabundant amount of fiber cannot be integrated in the structure.

During this work, the effects on structure's stiffness were disregarded, and a maximum length value was chosen for illustration purposes since the main objective was to compare the sensor performance metrics based on the FIM and the mFIM. The lengths chosen were 0.15 m for the isotropic test, and 3.5 m for the orthotropic ones (2D and 3D tests). The maximum length allowed in the orthotropic cases is an order of magnitude larger since the dimensions of the geometries used are 1 order of magnitude larger as well.

6.1.2. Minimum curvature radius

The minimum curvature radius is important for two main reasons: the fragility of optic fibers and the poor quality of readings one might obtain from a sharply bent fiber. For Bragg Grating optic fibers, there is a negligible impact on the readings for curvature radii of up to 3 cm [33]. Guyard et al. [34] demonstrated that this depends on the mean effective index of the fiber, obtaining negligible effects for as low as 1 cm for certain values. Because of this, a value of 1 cm for C_{lim} was chosen to perform the numerical simulations.

6.1.3. Distance between sensing points

Typically, if using a direct implementation of a B-Splines algorithm, the points might not be uniformly distributed along the curve. For Bragg Grating optic fibers this does not pose any problem, since the Bragg patterns can be applied anywhere along the fiber, even if there is a minimum distance that must be respected. However, the possibility to have equispaced sensing locations within the fiber was mainly considered, since it would enable us to study Rayleigh Backscattering optic fibers as well. The equispaced points were obtained through an interpolation of the original points.

6.1.4. Penalization coefficient

The value of k in (33) was obtained empirically. The calibration procedure will be demonstrated using the first test scenario, which involves optimizing an optical fiber designed to identify the Young modulus of an isotropic homogeneous plate under tension (as described in Section 7.1). For all cases, L_{lim} and C_{lim} were set to 0.15 m and 0.01 m respectively. The resulting fiber length and minimum radius obtained from the optimization process for different values of k are presented in Table 1.

In this scenario, it was observed that the fiber length was more sensitive to this penalization coefficient. Finally, a value of 4 was chosen since it resulted in variations lower than a millimeter in the length of the fiber with respect to L_{lim}.

6.2. Optimization steps

With the theory behind sensor performance metrics and the methodology for parametrizing the optic fiber now defined, the steps for optimizing sensor placement can be summarized in the form of an algorithm. Two different algorithms are presented: one based on the classical Fisher Information Matrix (8) and another using the modified Constitutive Relation Error (mCRE) and its associated modified Fisher Information Matrices (17), (30).

One of the main computational advantages of the classical FIM is that finite element simulations are performed independently of the information obtained from the optic fiber. This means that during the optimization process, only a projection of the previously computed parameter sensitivity fields is required. In contrast, the mCRE establishes a link between the measurements and the model to generate data-enriched admissible fields, as shown in (12). Consequently, different admissible fields must be constructed for each sensor configuration.

The optimization algorithm used for both approaches was differential evolution. It is a stochastic, population-based global optimization algorithm which belongs to the family of evolutionary algorithms. Differential evolution operates through the iterative improvement of a population of candidate solutions. In each generation, new candidate solutions are generated by combining existing ones according to a specific strategy, and only the fittest individuals are retained. A key advantage of differential evolution is that it does not rely on gradient information to guide the search; instead, it explores the search space using population dynamics. It was chosen since it has been previously validated in various optimal sensor placement publications [3,8,35]. A description of the algorithm and its hyper-parameters can be found in Annex A.4, however a curious reader can refer to [36] for an in-depth description. A general overview of the algorithm is shown in Fig. 7.

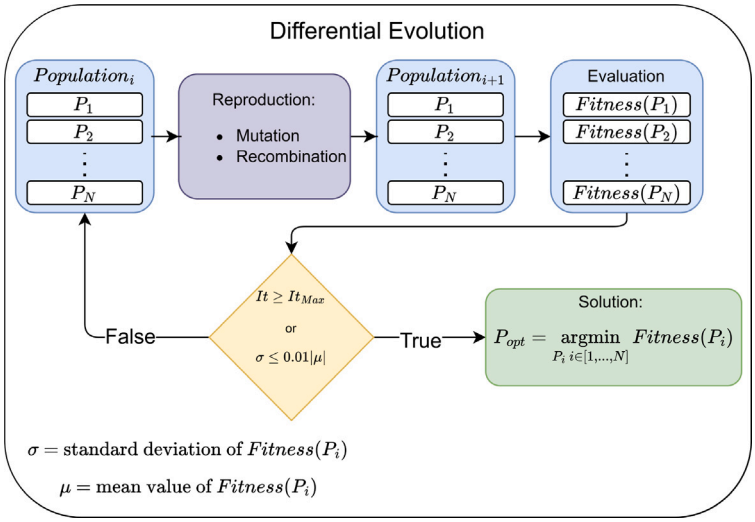

Fig. 7. Overview of the differential evolution algorithm.

6.2.1. Using the classical FIM

Algorithm 1 lists the necessary steps to perform the optimal sensor placement using the classical FIM. Quantities that are constant for all sensor configurations are computed during the initialization stage (including the sensibilities with respect to the constitutive parameters we wish to identify).

Algorithm 1 Optimal Sensor Placement

Initialize:
Perform finite element simulation of the loading case.
Calculate $\left(\frac{\partial U}{\partial \theta_i}\right)$ for all target parameters θ_i
Define the number of B-Spline control points.

Optimization of control polygon coordinates using differential evolution:
When the fitness function of a sensor arrangement is evaluated:
Generate B-Spline to define fiber path.
Compute length and min curvature radius.
Project constitutive parameter sensitivity results to fiber coordinates.
Build FIM (8).
Calculate cost function (33).

6.2.2. Using the modified FIM

Algorithm 2 lists the necessary steps to perform the optimal sensor placement with the modified FIM. We focus on the mechanical problem introduced in Section 3.

7. Sensor placement results using the modified FIM

The newly proposed modified mFIM2 (30) provides an indicator of the level of uncertainty in the solution of inverse problems using the mCRE. In this section, its effectiveness as a sensor performance metric is evaluated by comparing it to the classical FIM (8), and the mFIM1 (17) proposed by Diaz et al. [18], in a series of simple mechanical problems. An isotropic case is analyzed first, followed by two orthotropic ones (2D and 3D examples).

7.1. Isotropic homogeneous implementation

The case study involves placing the optic fiber in the 2D plate shown in Fig. 8. The plate is made of a linear, homogeneous, isotropic material subjected to a tensile load, with material properties defined as: Young's moduli E = 1 Pa, Poisson's ratio $\mu = 0.3$. A tensile load of 0.01 Pa is applied as a Neumann boundary condition on Γ_{N1}, while zero displacement is imposed on Γ_D. Measurement noise is set at 10% to compute $\mathbb{G}_{obs}$.

Algorithm 2 mCRE Optimal Sensor Placement

Initialize:
Define the variance of the added Gaussian noise.
Perform high fidelity FE simulation at the real parameters to use as U_{obs}
Define number of B-Spline control points.
Set initial weighting factor α_0: start with a random initial sensor configuration, or a configuration obtained from the classical FIM, and use it to set a preliminary value of α using the Morozov principle (15).

while $|\alpha_{i+1} - \alpha_i| \geq 0.01\alpha_i$ **do**
Optimization of control polygon coordinates using Differential evolution:
When the fitness function of a sensor arrangement is evaluated:
Generate B-Spline from control points coordinates.
Compute length and min curvature radius.
Obtain sensor data from high fidelity FE simulation U_{obs}.
Generate mCRE fields (12).
Build mFIM (30).
Calculate fitness function (33).
Update α_{i+1} using Morozov's principle.
end while

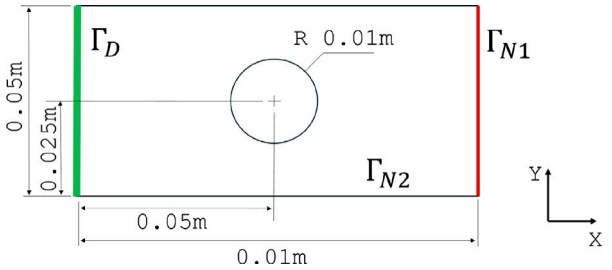

Fig. 8. Considered test case, with geometry and loading.

The goal is to determine an optimized sensor placement for identifying the Young modulus of the plate using the mCRE approach. Furthermore, since only one parameter is analyzed, the Fisher Information Matrix is a constant. Recall that a maximum length of 0.15 m and a minimum radius of 0.01 m are imposed as penalization terms. In addition, the starting point of the fiber is located on the surface Γ_D. To minimize the cost function (33), the differential evolution algorithm is used with a Sobol-distributed initial population, 1000 iterations, a recombination probability of 0.7, and a mutation factor varying between 1.1 and 1.9 (empirically determined, as is typical for global optimization algorithms).

The shape of the likelihood distribution based on the mCRE is highly sensitive to the value of α, and the same holds true for the modified FIMs. Limit values correspond to the classical least-squares minimization with no modeling error when $\alpha \to 0$ (equivalent to using the Gaussian distribution (4)), and to pure CRE minimization with prescribed experimental data when $\alpha \to \infty$ [30]. A parametric study with various values is first conducted to visualize its impact on the mFIM1 and mFIM2.

As $\alpha \to 0$, all cost functions (FIM, mFIM1, and mFIM2) yield the same value, resulting in the same optimized shape. This quickly changes as α increases, resulting in different sensor configurations as seen in Table 2. The variance of the identified parameter can then be used to compare the effectiveness of the sensor configurations. This can be achieved by comparing the curvature of the posterior distribution around the identified parameter, or conversely the Hessian of the mCRE for each sensor configuration. For all values of α analyzed, the mFIM2 yields the best results. However, the improvement in Hessian's magnitude is less than 10%, as seen in Table 3.

Now that the influence of α on mFIM1 and mFIM2 has been analyzed, its value can be calibrated according to the noise level. As detailed in Section 3.2, Morozov's principle is used for this calibration, leading to an optimal value of $\alpha = 10^{-9}$. The corresponding convergence curves are shown in Annex A.2. For this value, both mFIM1 and mFIM2 produce the same optimized sensor placement shape.

7.2. Orthotropic homogeneous implementation

For the orthotropic case, the geometry and boundary conditions are adjusted to enhance the simultaneous identification of the Young moduli in the X and Y directions (E1 and E2); see Fig. 9. Additionally, the maximum length is increased to 3.5 m and the noise level is reduced from 10% to 5% (to facilitate the parameter identification process). The plate is subjected to a tensile load,

Table 2
Comparison of results for different values of α.

α	FIM	mFIM1	mFIM2
1e-15	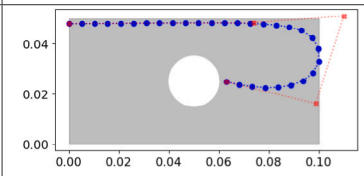	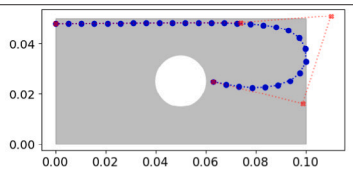	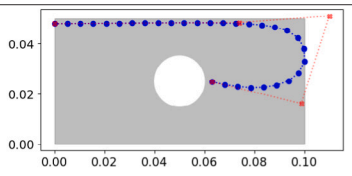
1e-9		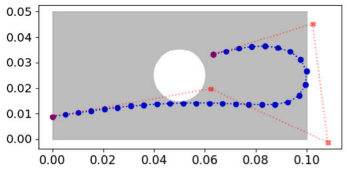	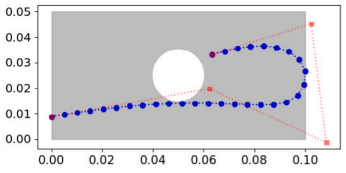
1e-8		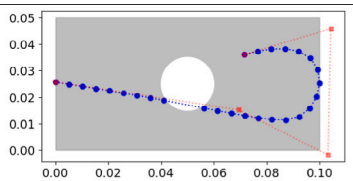	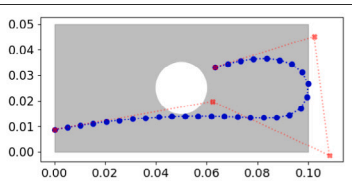
1e-7		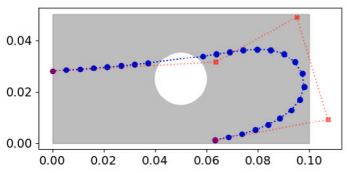	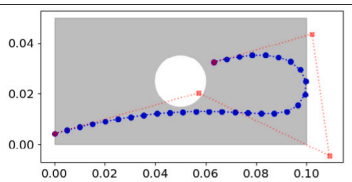

Table 3
Improvement in Hessian of the mCRE (compared to the sensor configuration obtained using the FIM).

α	Using mFIM1	Using mFIM2
1.00E−15	0%	0%
1.00E−09	4.89%	4.89%
1.00E−08	1.35%	5.11%
1.00E−07	1.48%	6.54%

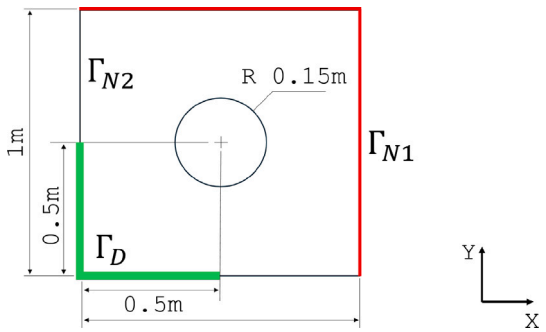

Fig. 9. Boundary conditions for the orthotropic case.

with material properties defined as: Young's moduli E1 = E2 = 1 Pa, Poisson's ratio $\mu = 0.3$. A tensile load of 0.01 Pa is applied as a Neumann boundary condition on Γ_{N1}, while zero displacement is imposed on Γ_D. Measurement noise is set at 5% to compute $\mathbb{G}_{obs}$.

These constitutive parameters lead to a displacement equivalent to that obtained using an isotropic constitutive law, but the sensitivity of the Young modulus in each direction can be evaluated independently. The goal is now to determine an optimized

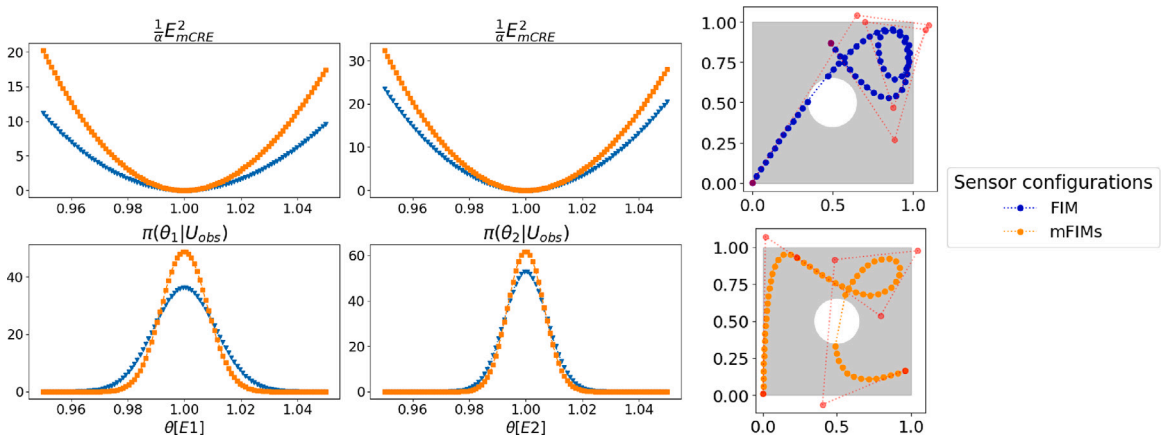

Fig. 10. Parameter identification and optimized fiber shape using FIM and mFIMs (mFIM1 and mFIM2).

Table 4
Improvement in Hessian of the mCRE for the orthotropic case (compared to the sensor configuration obtained using the FIM).

Improvement using mFIMs (both mFIM1 and mFIM2)	
E1	E2
45%	27%

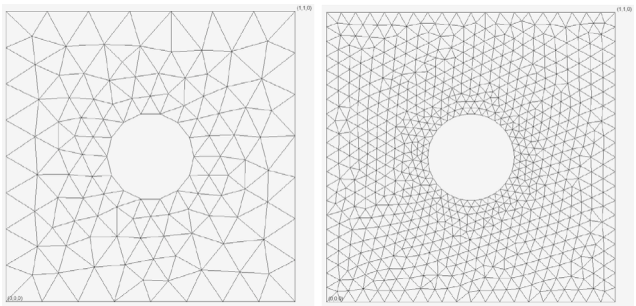

Fig. 11. Coarse mesh used for the model and fine mesh used to generate the data.

sensor placement for identifying E1 and E2 using the mCRE approach. Unlike the isotropic case, the Fisher Information Matrix (FIM) becomes a 2×2 matrix, so its determinant is used in the optimization algorithm.

Morozov's principle (15) is applied to adjust α once again during the optimization process, and a final value of 10^{-9} is reached. The corresponding convergence curves are shown in Annex A.2. The final shapes that result from the optimization process using the FIM and both modified versions, as well as the posterior distributions obtained with each sensor configuration are shown in Fig. 10. For this value of α, both mFIM1 (17) and mFIM2 (30) result in the same sensor configuration. The modified FIMs yield a superior sensor configuration for the mCRE, providing lower variance in the identified parameter, which we can verify numerically through the Hessian of the mCRE. The relative improvement is included in Table 4.

7.2.1. Introduction of modeling error

Until now, the "data" has been generated numerically by taking the response from the finite element model and adding Gaussian noise. However, with the mCRE, further advancements can be made to incorporate possible modeling errors, such as discretization errors or a constitutive law that does not perfectly match the material. Discretization errors are thus here incorporated into the model by utilizing two different meshes: a coarse mesh for the model and a finer mesh, that would better capture the stress concentrations near the hole, for generating the "data" as illustrated in Fig. 11. The noise percentage remains unchanged at 5%.

A slightly higher value of α is now needed to approach the noise level, with 5.10^{-8} compared to the 10^{-9} used previously. The corresponding convergence curves are shown in Annex A.2

The optimized shape for the classical FIM remains unchanged, a direct consequence of excluding modeling errors. In contrast, as α increases, different optimized shapes emerge for mFIM1 and mFIM2, consistent with the trends observed in Table 2. However,

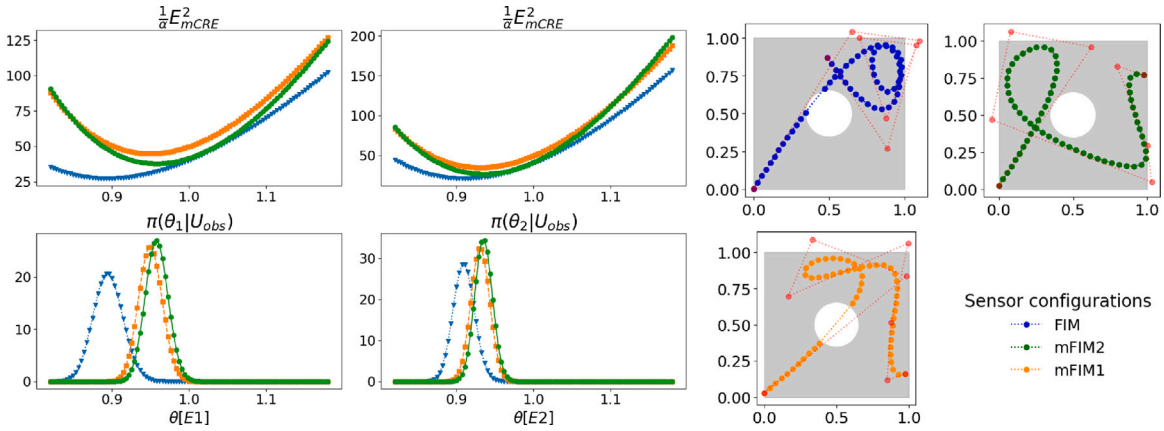

Fig. 12. Parameter identification and optimized fiber shape using FIM, mFIM1, and mFIM2.

Table 5
Improvement in Hessian of the mCRE for orthotropic case using different meshes (compared to the sensor configuration obtained using the FIM)

Improvement using mFIM1		Improvement using mFIM2	
E1	E2	E1	E2
19%	9%	34%	17%

Table 6
Identified parameters at various noise levels.

Noise	E1 [Pa]			E2 [Pa]		
	FIM	mFIM1	mFIM2	FIM	mFIM1	mFIM2
5%	0.896	0.947	0.957	0.912	0.932	0.937
10%	0.891	0.942	0.957	0.907	0.922	0.932
15%	0.891	0.932	0.957	0.907	0.917	0.932
20%	0.896	0.932	0.962	0.912	0.917	0.932

Table 7
Standard deviation of identified parameters at various noise levels.

Noise	E1 [Pa]			E [Pa]		
	FIM	mFIM1	mFIM2	FIM	mFIM1	mFIM2
5%	0.0194	0.0157	0.0148	0.0141	0.0122	0.0116
10%	0.0270	0.0235	0.0222	0.0194	0.0179	0.0168
15%	0.0327	0.0305	0.0285	0.0235	0.0226	0.0211
20%	0.0372	0.0362	0.0339	0.0267	0.0268	0.0251

the mFIM1 criterion considers only the distance to data portion of the mCRE functional (10), whereas mFIM2 accounts for both the distance to data and distance to model terms.

The optimized sensor positions obtained using FIM, mFIM1, and mFIM2 are presented in Fig. 12. The variance of the identified parameters serves as a performance indicator and can be quantitatively assessed through the Hessian of the mCRE for each parameter. This analysis confirms that mFIM2 yields the most effective sensor configuration, followed closely by mFIM1, as demonstrated in Table 5.

Additionally, it is observed that the optimal parameter estimate is no longer exactly 1, as a coarser mesh model is now being fitted, introducing a modeling bias. However, both mCRE-based sensor configurations (mFIM1 and mFIM2) exhibit a slight shift toward the true value of 1, improving parameter estimation despite the coarser mesh.

To verify the robustness of the sensor configuration found, the distances between sensing points were varied within the range from 0.03 m to 0.07 m and no difference in the obtained shape was found.

7.2.2. Robustness with respect to measurement noise

The robustness of the modified Constitutive Relation Error (mCRE) to observation noise is well established [15–17]. To examine whether this robustness extends to mCRE-based sensor placement, parameter identification at various noise levels (from 5% to 20% in steps of 5%) was carried out.

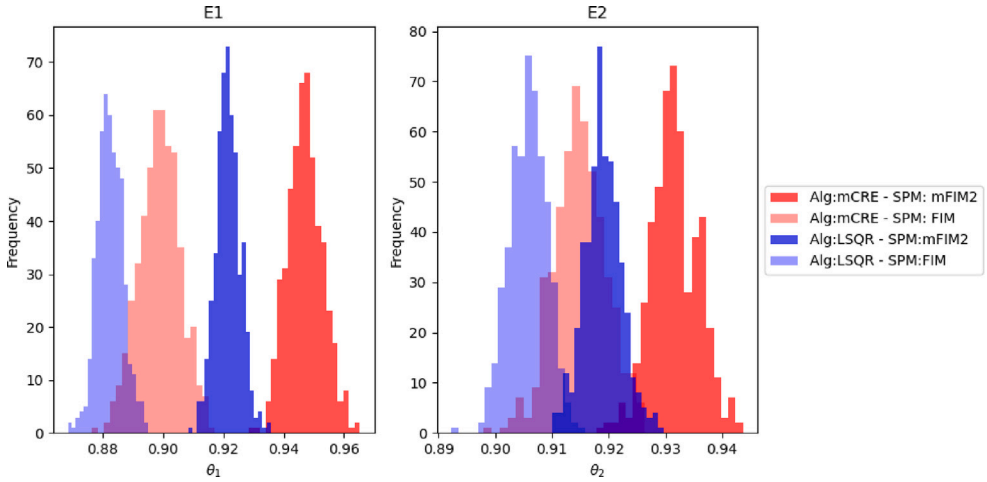

Fig. 13. Histogram of identified parameters using mCRE and least squares approach.

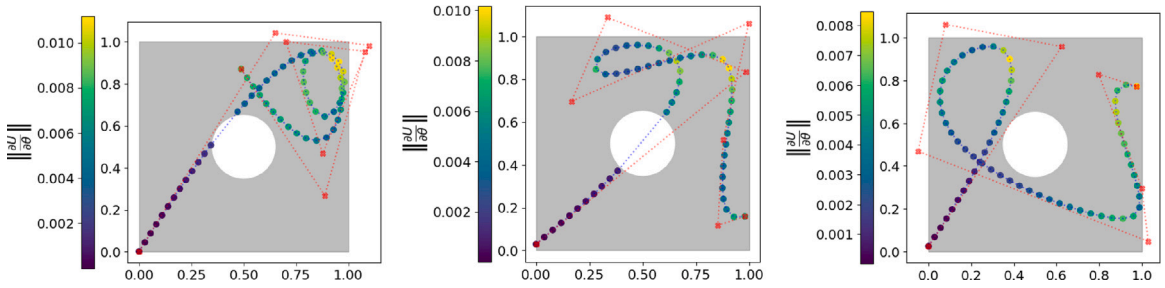

Fig. 14. $\frac{\partial U}{\partial \theta}$ local sensibility along the fiber path, configurations obtained using FIM, mFIM1, and mFIM2 respectively.

Table 8
Norm of local sensibility along the fiber.

$\frac{\partial U}{\partial \theta}$ Local sensibility norm		
FIM	mFIM1	mFIM2
0.05014	0.03885	0.03682

To assess the statistical significance, a one-way ANOVA test was performed on the estimated parameters. The test yielded a p-value close to zero for all noise levels, indicating a statistically significant difference in mean parameter estimates between at least some configurations. Among them, the mFIM2 configuration consistently produced estimates closest to the true value of 1 (as seen in Table 6), suggesting reduced modeling bias under mesh coarsening. It also achieved the lowest standard deviation across all noise levels (as seen in Table 7), highlighting its robustness not only to numerical modeling error but also to observation noise.

7.2.3. Comparison with classical least square approaches

To further assess the effectiveness of mFIM2 in achieving parameter identification closer to the true value of 1, even in the presence of model bias from the coarse mesh, a histogram of the identified parameter values over 500 trials is presented in Fig. 13. This histogram compares results obtained using both the mCRE and classical least squares methods, with sensor configurations derived from either the FIM or mFIM2. The results show that the sensor configuration based on mFIM2, when combined with the mCRE, yields parameter estimates closer to 1. In contrast, the configuration based on the FIM, used with the least squares approach, produces estimates that deviate further from the true value.

7.2.4. Global and local parameter sensitivity

To construct the FIM and the mCRE variants (mFIM1 and mFIM2), it is necessary to evaluate the sensibility with respect to θ. Fig. 14 shows the magnitude of $\frac{\partial U}{\partial \theta}$ at the sensing locations along the fiber path. It was noted that the configuration that provided the highest norm along the whole fiber corresponds to the FIM as seen in Table 8. This is indeed expected since the FIM maximizes the information that can be obtained from the modeling information alone.

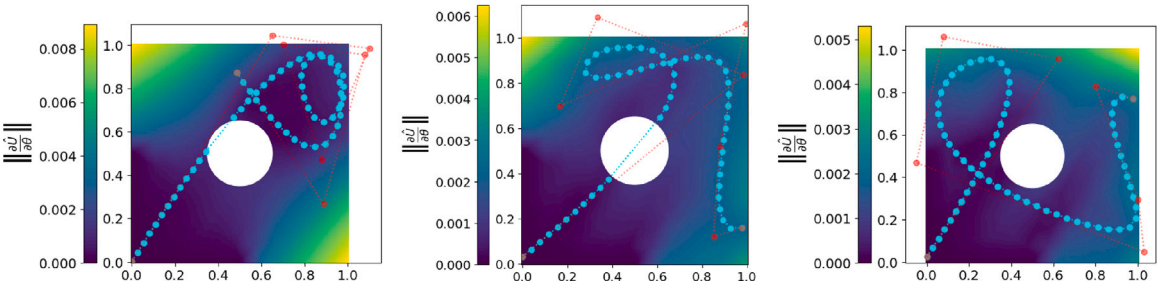

Fig. 15. $\frac{\partial \hat{U}}{\partial \theta}$ field on the plate, configurations obtained using FIM, mFIM1, and mFIM2 respectively.

Table 9
Norm of global sensibility on the whole plate.

$\frac{\partial \hat{U}}{\partial \theta}$ Global sensibility norm		
FIM	mFIM1	mFIM2
0.03382	0.02086	0.01667

However, the newly proposed mFIM2 involves the evaluation of global quantities that account for the entire structure, rather than focusing solely on local evaluations at the sensor positions. For this reason, the sensitivity of the mCRE field $\hat{U}$, which is the only quantity dependent on the sensor configuration, is also analyzed. Fig. 15 illustrates the field $\frac{\partial \hat{U}}{\partial \theta}$ over the plate for all configurations, while the norms of these fields are presented in Table 9.

In contrast to the relationship between the FIM and local sensitivity, the mFIM2 minimizes $\frac{\partial \hat{U}}{\partial \theta}$ across the plate. Two limiting cases can be identified: first, $\frac{\partial \hat{U}}{\partial \theta} \to 0$, which corresponds to prescribed observation values everywhere (achieved with $\alpha \to \infty$ and sensors distributed throughout the structure); and second, $\frac{\partial \hat{U}}{\partial \theta} \to \frac{\partial U}{\partial \theta}$, which occurs when no data is incorporated (either no sensing location, or $\alpha = 0$). This explains why the mFIM2 provides a sensor configuration that extends across the entire structure, covering a larger area, whereas the classical FIM can yield sensor placements concentrated in the most sensitive regions.

More formally, the relationship between $\frac{\partial \hat{U}}{\partial \theta}$ and the mFIM2 (30) can be described as follows:

$$mFIM2 \propto \hat{U}^{0^T} \frac{\partial \mathbb{K}}{\partial \theta} \frac{\partial \hat{U}^0}{\partial \theta} - \hat{V}^T \frac{\partial \mathbb{K}}{\partial \theta} \frac{\partial \hat{V}}{\partial \theta}$$

From (12) $\to \hat{V} = U$ thus: (34)

$$mFIM2 \propto \hat{U}^{0^T} \frac{\partial \mathbb{K}}{\partial \theta} \frac{\partial \hat{U}^0}{\partial \theta} - U^T \frac{\partial \mathbb{K}}{\partial \theta} \frac{\partial U}{\partial \theta}$$

First term:

$$\begin{aligned} \hat{U}^{0^T} \frac{\partial \mathbb{K}}{\partial \theta} \frac{\partial \hat{U}^0}{\partial \theta} &= \hat{U}^{0^T} \frac{\partial \mathbb{K}}{\partial \theta} \left[-(\mathbb{K} + \alpha \Pi^T G_{obs} \Pi)^{-1} \frac{\partial \mathbb{K}}{\partial \theta} \hat{U}^0 \right] \\ \hat{U}^{0^T} \frac{\partial \mathbb{K}}{\partial \theta} \frac{\partial \hat{U}^0}{\partial \theta} &= -\hat{U}^{0^T} \frac{\partial \mathbb{K}}{\partial \theta} (\mathbb{K} + \alpha \Pi^T G_{obs} \Pi)^{-1} \frac{\partial \mathbb{K}}{\partial \theta} \hat{U}^0 \end{aligned} \tag{35}$$

Second term:

$$\begin{aligned} -U^T \frac{\partial \mathbb{K}}{\partial \theta} \frac{\partial U}{\partial \theta} &= -U^T \frac{\partial \mathbb{K}}{\partial \theta} \left[-\mathbb{K}^{-1} \frac{\partial \mathbb{K}}{\partial \theta} U \right] \\ -U^T \frac{\partial \mathbb{K}}{\partial \theta} \frac{\partial U}{\partial \theta} &= U^T \frac{\partial \mathbb{K}}{\partial \theta} \mathbb{K}^{-1} \frac{\partial \mathbb{K}}{\partial \theta} U \end{aligned} \tag{36}$$

The mFIM2 (30) has two terms, which depend on the sensibility of the mCRE field $\hat{U}^0$ and the finite element solution U. From these, only the first is dependent on the sensor layout. If we disregard rigid body modes (considered by the Dirichlet boundary conditions), the stiffness matrix $\mathbb{K}$ is symmetric positive definite. In addition, if G_{obs} is also positive definite (in our case it is since $G_{obs} = \Sigma_{obs}^{-1}$ and $\Sigma_{obs} = \sigma_{obs}^2 \mathbb{I}$), then $\Pi^T G_{obs} \Pi$ is at least positive semi-definite (positive definite if Π is full column rank). This means that the first term is negative definite, and the second term is positive definite. The objective is then to choose sensors such that the negative definite portion (35) is minimized, which is related to minimizing the global sensitivity of the term $\frac{\partial \hat{U}}{\partial \theta}$.

7.2.5. Influence of the ratio between the Young moduli in X/Y directions

The ratio between E1 and E2 was previously maintained at a value of 1. To visualize the impact on optimal sensor placement, this ratio was varied from 0.5 to 2. Table 10 presents the resulting configurations obtained using both FIM and mFIM2. For the FIM, the sensor placement changed across all three configurations, although the fiber path remained concentrated within the same region. For mFIM2, the sensor placement was slightly altered when E1/E2 = 0.5, but greatly altered when E1/E2 = 2. Therefore, while a reference ratio of 1 between E1 and E2 can be used to calibrate sensor placement, incorporating additional prior knowledge of the parameter's value may further optimize the sensor's location.

Table 10
Influence in ratio of Young's moduli.

Sensor performance metric	E1/E2 = 0.5	E1/E2 = 1	E1/E2 = 2
FIM	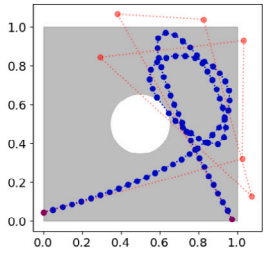	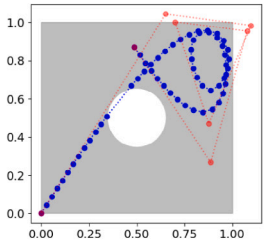	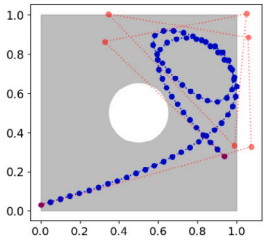
mFIM2	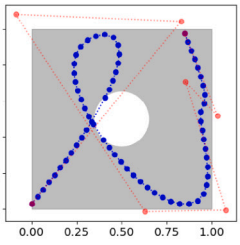	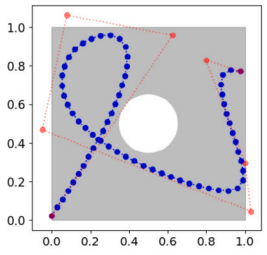	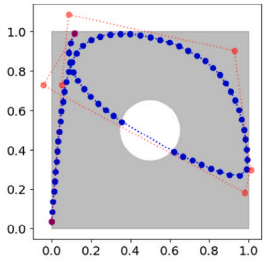

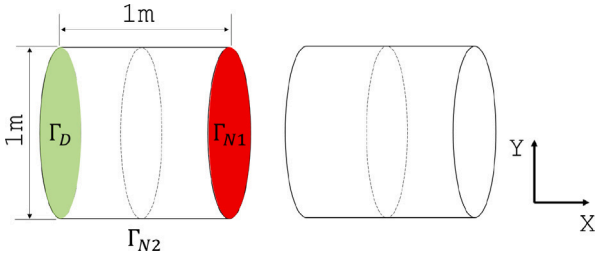

Fig. 16. Boundary conditions and target surface to place the optic fiber.

Table 11
Improvement in Hessian of the mCRE for 3D orthotropic test (compared to the sensor configuration obtained using the FIM).

Improvement using mFIM2		
E1	E2	E3
7%	11%	4%

7.3. Implementation on 3D curved surface

7.3.1. Cylinder subjected to bending

The procedure is now applied to a simple curved 3D geometry. A geometry made from an orthotropic homogeneous material, as shown in Fig. 16, is analyzed. This geometry consists of a cylinder with a fixed end, subjected to bending. Additionally, the cylinder's outer curved surface is selected as the target for the placement of the optic fiber.

The material properties are defined as follows: the Young moduli E1 = E2 = E3 = 1 Pa (X, Y, and Z directions), with a Poisson ratio of $\nu = 0.3$ and a shear modulus of 0.38 Pa. A bending load of 0.01 Pa is applied orthogonally to the surface as a Neumann boundary condition on Γ_{N1}, while a zero displacement condition is imposed as a Dirichlet boundary condition on Γ_D. Measurement noise is set at 5% for computing $\mathbb{G}_{obs}$.

Morozov's principle (15) was applied once again during the optimization process to adjust α, resulting in a final value of 6.10^{-8}. The corresponding convergence curves are shown in Annex A.2. The final shapes resulting from the optimization process using both the FIM and mFIM2 are shown in Fig. 17. A comparative analysis of the mCRE Hessian improvement achieved through mFIM2-based sensor placement over the FIM approach is presented in Table 11.

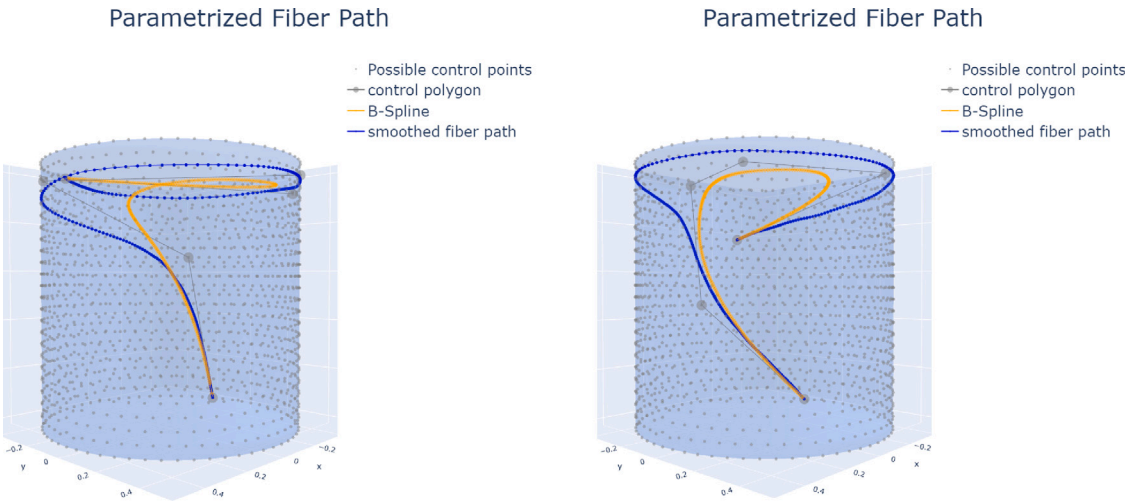

Fig. 17. Optimized shapes obtained with FIM and mFIM2 respectively.

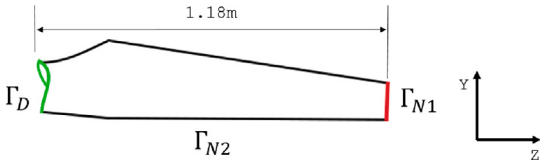

Fig. 18. Boundary conditions on the wind turbine blade.

7.3.2. Wind turbine blade subjected to bending

This methodology was also tested on the wind turbine blade geometry shown in Fig. 18 to verify its effectiveness. The same boundary conditions and constitutive parameters as those of the cylinder were used.

A value of 6.10^{-7} is reached for α, the corresponding convergence curves are shown in Annex A.2. For this geometry, the sensitivity with respect to E3 was significantly higher compared to E1 and E2, being approximately four orders of magnitude larger. In this illustrative example, the highly sensitive parameter was chosen to place the fiber, resulting in an 8% improvement in the Hessian of the mCRE, compared to the configuration obtained using the FIM. The final shapes resulting from the optimization process using both the FIM and mFIM2 are shown in Fig. 19. It is worth noting that for this particular geometry, the curvature constraint plays a critical role, as it prevents the fiber from reaching surface regions where the local curvature exceeds the specified threshold.

7.3.3. Computational cost

One of the main constraints of the mCRE and the sensor performance metric introduced in this paper is the computational cost, particularly when dealing with 3D geometries. For example, when considering the wind turbine blade mesh (comprising 9258 nodes), the computational time to evaluate the performance of a single sensor configuration using the mFIM2 is 0.418 s, whereas the FIM requires only 0.047 s (times obtained using a single Sky Lake node). This difference becomes especially significant when a genetic algorithm, such as differential evolution, is used, as the cost function may need to be evaluated thousands of times, depending on the population size and number of iterations. A runtime profiler was employed to measure the runtime distribution for both the FIM and mFIM2, with the results shown in Fig. 20. For the FIM, it is evident that the task requiring the most time is the generation of the projection matrix Π to obtain information at the sensor locations. In contrast, for the mFIM2, the LU decomposition, necessary for computing the mCRE admissible fields, dominates the runtime.

8. Conclusions

Based on the results obtained in this work, several conclusions can be drawn. Regarding the parametrization of the optical fiber in a 2D plane, B-Splines are identified as an efficient solution since only the coordinates of the control points are required. Other techniques have been used [3,20], but these require both coordinates and derivative values for subsequent interpolation. The use of B-Splines was also extended to treat any generic smooth surface through the use of an orthogonal projection of the B-Spline path to the surface.

For optimal sensor placement, metrics based on the Fisher Information Matrix (FIM) can be safely utilized, as they are directly related to the variance of the identified parameters, with this matrix being dependent on the sensor configuration. Concerning the

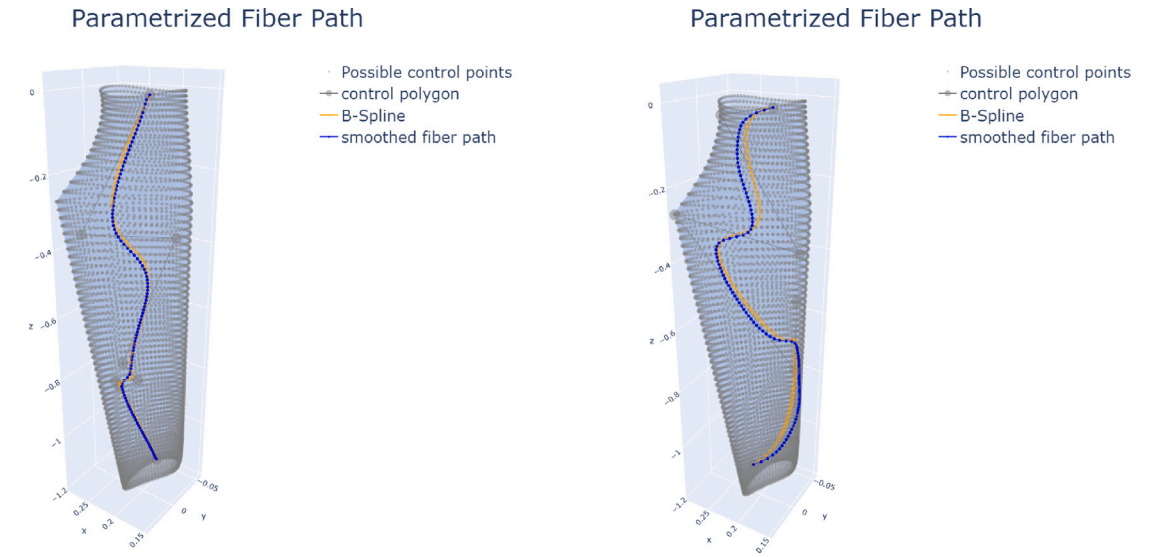

Fig. 19. Optimized shapes obtained with FIM and mFIM2 respectively.

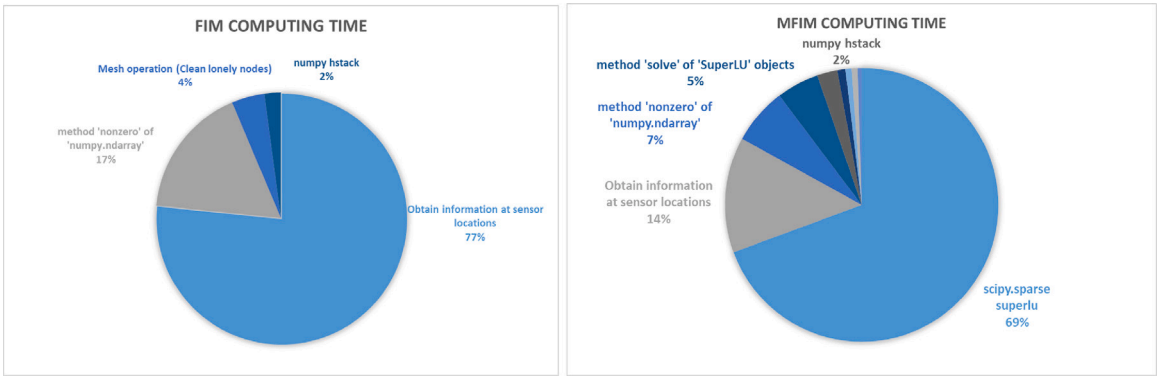

Fig. 20. Computational time percentage for FIM and mFIM.

modified FIM introduced in this work (30), it was shown that it can be used as a sensor performance indicator tailored for the mCRE approach. In addition, possible modeling errors and measurement noise values can be explored and incorporated directly in the sensor placement problem. It was also shown that the FIM is a local indicator, that depends only on the information at the sensor locations. On the other hand, the newly proposed mFIM2 depends on the global sensibility of the mCRE fields.

Compared to the already existent mFIM1, the newly proposed mFIM2 can be reliably used to maximize the Hessian of the mCRE for all values of α. In contrast, the mFIM1 can only optimize the Hessian if distance to data portion of the mCRE takes a greater importance, or conversely when the value of α is sufficiently low (the exact value is bounded to the noise level, quality of the model, etc.).

However, the mFIM2 has its drawbacks, mainly the added complexity of computing the admissible fields. Since these admissible fields depend on the sensor configuration, they must be evaluated multiple times during the optimization algorithm. Fortunately, genetic algorithms such as differential evolution can be effectively parallelized. In addition, model order reduction techniques could also be employed to reduce the computation time required to generate the mCRE fields. Improvements in the solution of the linear system itself can also be envisioned, as it accounts for the majority of the computation time. A possible approach is to isolate the term dependent on the sensor locations through the use of the Sherman–Morrison–Woodbury formula [37]. All of these are topics of future research works.

While this study focused on the theoretical formulation and numerical demonstration of the mFIM2 for sensor placement, future work will address its integration into practical composite monitoring scenarios. This includes the incorporation of physical constraints specific to composite structures, such as manufacturing-induced variability, or the interlayer integration of fiber-optic sensors during layup [38]. Defining the operational boundaries of the proposed method, including maximum detectable damage size, strain resolution, and sensor survivability, are also necessary to ensure effective real-world deployment [32]. These aspects will be

explored in future research to transition from a numerical optimization framework to an end-to-end SHM solution for advanced composite structures.

CRediT authorship contribution statement

José Andrés Pérez Orozco: Writing – original draft, Software, Methodology, Investigation, Formal analysis, Conceptualization. **Ludovic Chamoin:** Writing – review & editing, Supervision, Methodology, Investigation, Funding acquisition, Conceptualization. **Julien Cortial:** Writing – review & editing, Supervision, Methodology, Investigation, Funding acquisition, Conceptualization. **Maya de Buhan:** Writing – review & editing, Supervision, Methodology, Investigation, Conceptualization. **Bruno Soulier:** Writing – review & editing, Supervision, Methodology, Investigation, Conceptualization.

Declaration of competing interest

The authors declare that they have no known competing financial interests or personal relationships that could have appeared to influence the work reported in this paper.

Acknowledgments

This work has received funding from the European Research Council (ERC) under the European Union's Horizon 2020 research and innovation programme-ERC-2020-COG-ERC Consolidator Grant (Grant Agreement No. 101002857, DREAM-ON Project).

Annex

A.1. Hessian form of the FIM

Here we give necessary developments to prove that expressions (5) and (6) are equivalent. First we can relate the derivative of a pdf and the derivative of the logarithm of a probability density function as follows:

$$\frac{\partial \pi(x;\theta)}{\partial \theta} = \frac{\partial ln\pi(x;\theta)}{\partial \theta}\pi(x;\theta) \tag{37}$$

If we compute the second derivative:

$$\begin{aligned}\frac{\partial^2 ln\pi(x;\theta)}{\partial \theta^2} &= \frac{\partial^2 \pi(x;\theta)}{\partial \theta^2}\frac{1}{\pi(x;\theta)} - \left[\frac{\partial \pi(x;\theta)}{\partial \theta}\frac{1}{\pi(x;\theta)}\right]^2 \\ \frac{\partial^2 ln\pi(x;\theta)}{\partial \theta^2} &= \frac{\partial^2 \pi(x;\theta)}{\partial \theta^2}\frac{1}{\pi(x;\theta)} - \left[\frac{\partial ln\pi(x;\theta)}{\partial \theta}\right]^2\end{aligned} \tag{38}$$

Now we take the expectation on both sides as follows:

$$\begin{aligned}\mathbb{E}\left[\frac{\partial^2 ln\pi(x;\theta)}{\partial \theta^2}\right] = &\underbrace{\mathbb{E}\left[\frac{\partial^2 \pi(x;\theta)}{\partial \theta^2}\frac{1}{\pi(x;\theta)}\right]}_{} - \mathbb{E}\left[\left(\frac{\partial ln\pi(x;\theta)}{\partial \theta}\right)^2\right] \\ \mathbb{E}\left[\frac{\partial^2 \pi(x;\theta)}{\partial \theta^2}\frac{1}{\pi(x;\theta)}\right] &= \int \frac{\partial^2 \pi(x;\theta)}{\partial \theta^2}\frac{\pi(x;\theta)}{\pi(x;\theta)}dx \\ &= \int \frac{\partial^2 \pi(x;\theta)}{\partial \theta^2}dx \\ &\downarrow \text{Leibniz Rule} \\ &= \frac{d^2}{d\theta^2}\underbrace{\int \pi(x;\theta)dx}_{1} = 0\end{aligned} \tag{39}$$

Thus,

$$\mathbb{E}\left[\frac{\partial^2 ln\pi(x;\theta)}{\partial \theta^2}\right] = -\mathbb{E}\left[\left(\frac{\partial ln\pi(x;\theta)}{\partial \theta}\right)^2\right]$$

A.2. Calibration of alpha

Table 12 presents the graphs used to calibrate the value of α for the studies discussed in this work.

Table 12
Calibration of α for the different studies.

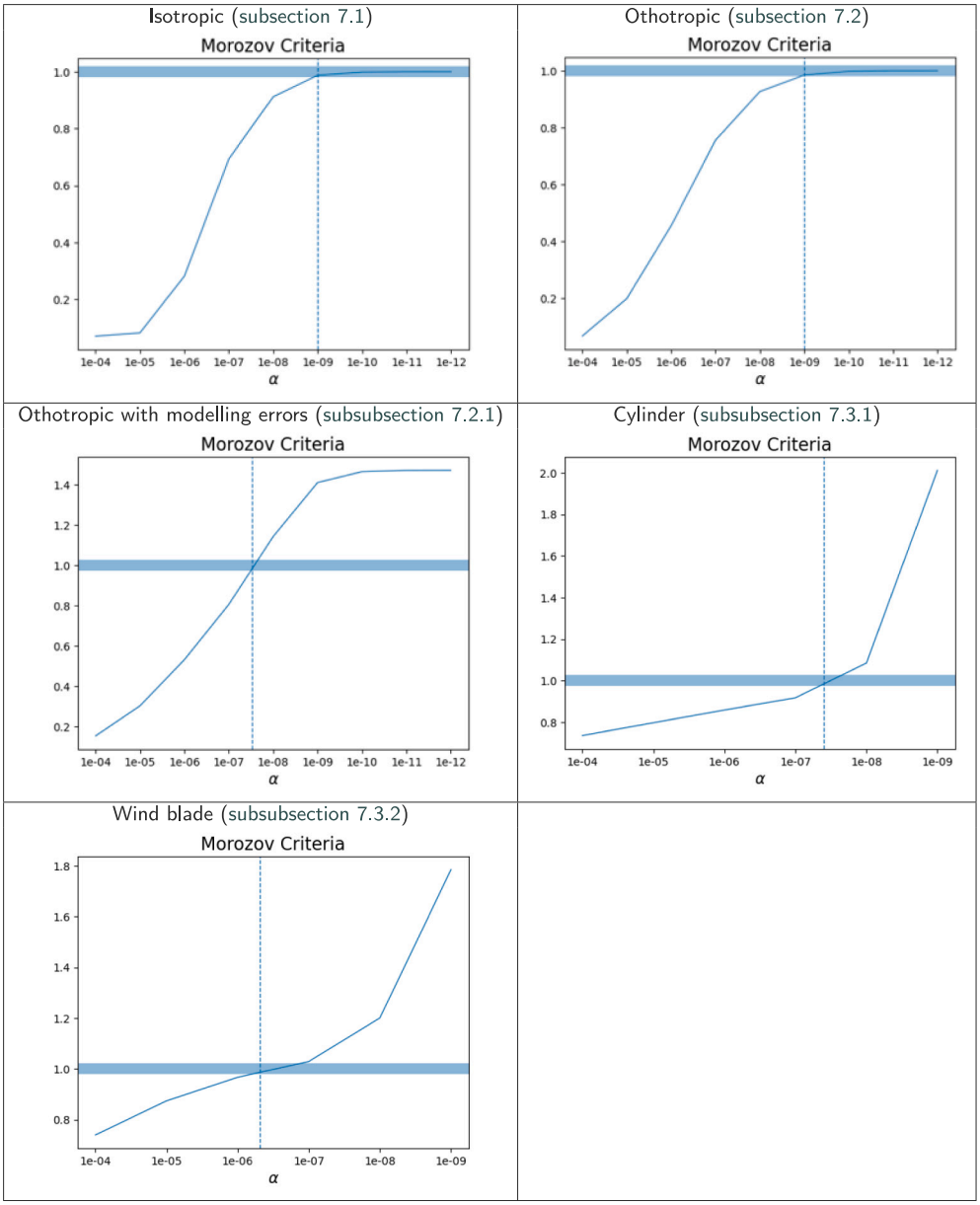

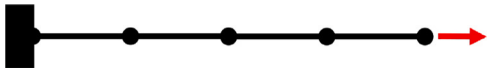

Fig. 21. 1D bar under tension.

A.3. Illustration of the impact of the value of α

The impact of the value of α in the mCRE can be illustrated with a simple example of a 1D beam under tension with a homogeneous Young modulus to be identified, as shown in Fig. 21. The observed displacement values at the nodes (U_{obs}) were generated by adding a Gaussian noise of 50% to a finite element solution (to better visualize the difference).

The percentage that the distance to data and distance to model (10) portions take in the mCRE for different values of α, and the manner data enriched field $\hat{U}$ behaves at the two limits is shown in Figs. 22 and 23 respectively.

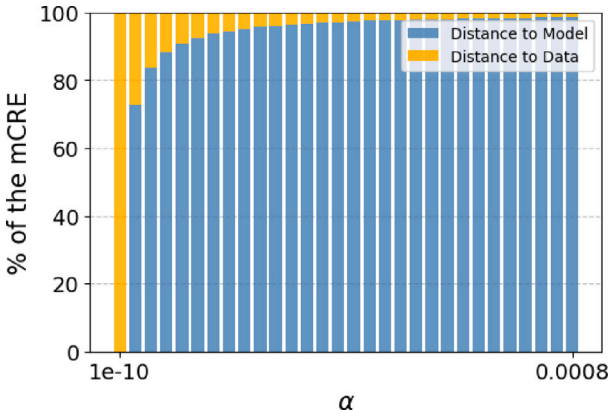

Fig. 22. Distance to data and distance to model percentages in the mCRE.

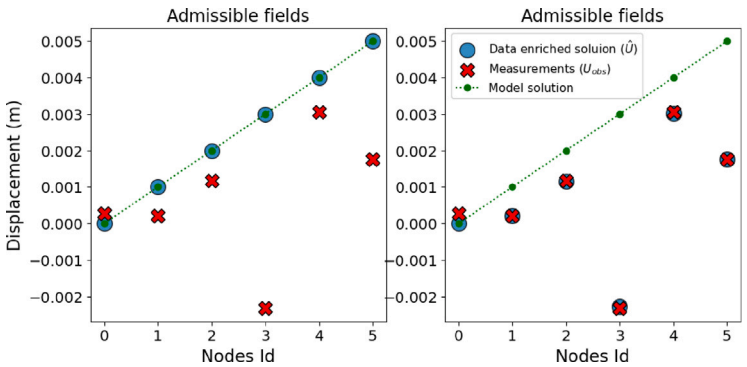

Fig. 23. Behavior of $\hat{U}$ at limit α values.

Low values of α correspond to high confidence in the model. In this case the data enriched field $\hat{U}$ is not influenced by the measurements, and the biggest portion of the mCRE is equal to the distance to data portion. On the other hand, high values of α correspond to confidence in the data. The measurements are now prescribed in the data enriched field $\hat{U}$, and the biggest portion of the mCRE is equal to the distance to model portion.

A.4. Differential evolution

Most of the current publications define a discrete and finite number of possible sensor locations, and to determine the optimal positions, evolutionary algorithms [3,8] and sequential sensor placement (SSP) algorithms [12] have proven themselves as viable options. Evolutionary algorithms can also be used however, to solve continuous optimization problems, unlike SSP algorithms that require to iterate over the possible locations.

Differential Evolution is one of the most popular evolutionary algorithms for solving optimization problems over a continuous space. In a simple differential evolution, the following components can be defined [36]:

- Population: Consists of NP individuals. Each individual is represented by the vector $x_i = (x_{1,i}, x_{2,i}, \dots, x_{D,i})$, where $i \in [1, NP]$ and D is the dimension of the solution space. There are various methods that define how the initial population is distributed, the default option in the SciPy algorithm is the Latin Hypercube Sampling, but it is stated that Sobol provides superior performance which also enforces an initial population size [39]. For this reason, it was the chosen initialization strategy in this work.
- Generation: Are the iterations of the algorithm.
- Bounds: Upper and lower bounds for each of the variables to optimize.
- Mutation: Mechanism that constructs the mutation vectors, which are used to modify the current individuals. There are various mutation strategies, from completely random to guided, and define behavior the algorithm will have in the search for new solutions.
- Crossover: Mechanism that defines how the current individuals will be combined with the mutation vector to generate a new candidate solution (trial vector). There are two main types: binomial and exponential. Binomial is the most stable, and it alters a value of an individual by taking the value of the mutation vector based on a probability defined by the user. In [36]

it was stated that 0.8 is the maximum value of crossover probability that can maintain a balance between exploration and a more local search. The default value proposed by the SciPy algorithm is slightly smaller at 0.7 to provide a more stable approach [39].

- Fitness function: Cost function to be optimized
- Selection: Differential evolution adapts a greedy selection strategy. If and only if the trial vector yields as good as or a better fitness function value that the current solution, then it will be taken as the new solution.
- Stopping criteria: Standard deviation of population is smaller than a certain tolerance or a maximum number of iterations is reached.

Data availability

Data will be made available on request.

References

[1] C.R. Farrar, K. Worden, An introduction to structural health monitoring, Philos. Trans. R. Soc. A: Math. Phys. Eng. Sci. 365 (1851) (2007) 303–315.
[2] A. Güemes, A. Fernandez-Lopez, A.R. Pozo, J. Sierra-Perez, Structural health monitoring for advanced composite structures: a review, J. Compos. Sci. 4 (1) (2020) 13.
[3] G. Cazzulani, M. Chieppi, A. Colombo, P. Pennacchi, Optimal sensor placement for continuous optical fiber sensors, in: Sensors and Smart Structures Technologies for Civil, Mechanical, and Aerospace Systems 2018, Vol. 10598, SPIE, 2018, pp. 970–981.
[4] D.C. Kammer, M.L. Tinker, Optimal placement of triaxial accelerometers for modal vibration tests, Mech. Syst. Signal Process. 18 (1) (2004) 29–41.
[5] A. Mardanshahi, A. Sreekumar, X. Yang, S.K. Barman, D. Chronopoulos, Sensing techniques for structural health monitoring: A state-of-the-art review on performance criteria and new-generation technologies, Sens. 25 (5) (2025) 1424.
[6] C. Yang, Y. Xia, A novel two-step strategy of non-probabilistic multi-objective optimization for load-dependent sensor placement with interval uncertainties, Mech. Syst. Signal Process. 176 (2022) 109173.
[7] C. Yang, H. Ouyang, A novel load-dependent sensor placement method for model updating based on time-dependent reliability optimization considering multi-source uncertainties, Mech. Syst. Signal Process. 165 (2022) 108386.
[8] J. Li, R.K. Kapania, W.B. Spillman Jr., Placement optimization of distributed-sensing fiber optic sensors using genetic algorithms, AIAA J. 46 (4) (2008) 824–836.
[9] J.A. Sharp, A.P. Browning, K. Burrage, M.J. Simpson, Parameter estimation and uncertainty quantification using information geometry, J. R. Soc. Interface 19 (189) (2022) 20210940.
[10] G.F. Gomes, S.S. da Cunha, P. da Silva Lopes Alexandrino, B. Silva de Sousa, A.C. Ancelotti, Sensor placement optimization applied to laminated composite plates under vibration, Struct. Multidiscip. Optim. 58 (2018) 2099–2118.
[11] F.E. Udwadia, Methodology for optimum sensor locations for parameter identification in dynamic systems, J. Eng. Mech. 120 (2) (1994) 368–390.
[12] C. Papadimitriou, Optimal sensor placement methodology for parametric identification of structural systems, J. Sound Vib. 278 (4–5) (2004) 923–947.
[13] W. Aquino, M. Bonnet, Analysis of the error in constitutive equation approach for time-harmonic elasticity imaging, SIAM J. Appl. Math. 79 (3) (2019) 822–849.
[14] S. Andrieux, Bregman divergences for physically informed discrepancy measures for learning and computation in thermomechanics, Comptes Rendus. Mécanique 351 (G1) (2023) 59–81.
[15] P. Feissel, O. Allix, Modified constitutive relation error identification strategy for transient dynamics with corrupted data: The elastic case, Comput. Methods Appl. Mech. Engrg. 196 (13–16) (2007) 1968–1983.
[16] P.-E. Charbonnel, P. Ladevèze, F. Louf, C. Le Noach, A robust CRE-based approach for model updating using in situ measurements, Comput. Struct. 129 (2013) 63–73.
[17] P. Ladevèze, D. Leguillon, Error estimate procedure in the finite element method and applications, SIAM J. Numer. Anal. 20 (3) (1983) 485–509.
[18] M. Diaz, P.-É. Charbonnel, L. Chamoin, Merging experimental design and structural identification around the concept of modified Constitutive Relation Error in low-frequency dynamics for enhanced structural monitoring, Mech. Syst. Signal Process. 197 (2023) 110371.
[19] P. Antunes, H. Lima, N. Alberto, L. Bilro, P. Pinto, A. Costa, H. Rodrigues, J. Pinto, R. Nogueira, H. Varum, et al., Optical sensors based on fiber Bragg gratings for structural health monitoring, New Dev. Sens. Technol. Struct. Heal. Monit. (2011) 253–295.
[20] S. Ameduri, M. Ciminello, I. Dimino, A. Concilio, A. Catignani, R. Mancinelli, Distributed sensor placement optimization for computer aided structural health monitoring, Arch. Mech. Eng. 66 (1) (2019) 111–127.
[21] A. Tarantola, Inverse Problem Theory and Methods for Model Parameter Estimation, SIAM, 2005.
[22] G.F. Gomes, F.A. de Almeida, P. da Silva Lopes Alexandrino, S.S. da Cunha, B.S. de Sousa, A.C. Ancelotti, A multiobjective sensor placement optimization for SHM systems considering Fisher information matrix and mode shape interpolation, Eng. Comput. 35 (2019) 519–535.
[23] E.L. Lehmann, G. Casella, Theory of Point Estimation, Springer Science & Business Media, 2006.
[24] H.N. Nguyen, L. Chamoin, Model and mesh selection from a mCRE functional in the context of parameter identification with full-field measurements, Comput. Mech. 76 (2025) 251–277.
[25] J. Lepine, F. Guibault, J.-Y. Trepanier, F. Pepin, Optimized nonuniform rational B-spline geometrical representation for aerodynamic design of wings, AIAA J. 39 (11) (2001) 2033–2041.
[26] C. Yang, Q. Yu, Multi-objective optimization-inspired set theory-based regularization approach for force reconstruction with bounded uncertainties, Comput. Methods Appl. Mech. Engrg. 438 (2025) 117814.
[27] P. Ladevèze, L. Chamoin, The constitutive relation error method: A general verification tool, in: Verifying Calculations-Forty Years On: An Overview of Classical Verification Techniques for FEM Simulations, Springer, 2016, pp. 59–94.
[28] P. Ladevèze, A. Chouaki, Application of a posteriori error estimation for structural model updating, Inverse Problems 15 (1) (1999) 49.
[29] A. Deraemaeker, P. Ladevèze, T. Romeuf, Model validation in the presence of uncertain experimental data, Eng. Comput. 21 (8) (2004) 808–833.
[30] H.N. Nguyen, L. Chamoin, C. Ha Minh, mCRE-based parameter identification from full-field measurements: Consistent framework, integrated version, and extension to nonlinear material behaviors, Comput. Methods Appl. Mech. Engrg. 400 (2022) 115461.
[31] V. Morozov, The error principle in the solution of operational equations by the regularization method, Comput. Math. Math. Phys. 8 (2) (1968) 63–87.

[32] L. Chamoin, S. Farahbakhsh, M. Poncelet, An educational review on distributed optic fiber sensing based on Rayleigh backscattering for damage tracking and structural health monitoring, Meas. Sci. Technol. 33 (12) (2022) 124008.
[33] P. Ferdinand, Capteurs a fibres optiques a reseaux de Bragg: Fabrication et caracteristiques, Tech. de Ing. 6735 (Dec) (2018) 1–24.
[34] R. Guyard, D. Leduc, Y. Lecieux, C. Lupi, J. Potet, J. Beauce, M. Douay, L. Lablonde, Reponse des reseaux de Bragg fibres a la courbure, Instrum. Mes. Metrol. 16 (2017).
[35] C. Yang, An adaptive sensor placement algorithm for structural health monitoring based on multi-objective iterative optimization using weight factor updating, Mech. Syst. Signal Process. 151 (2021) 107363.
[36] A.W. Mohamed, A.A. Hadi, A.K. Mohamed, Differential evolution mutations: taxonomy, comparison and convergence analysis, IEEE Access 9 (2021) 68629–68662.
[37] B. Marchand, L. Chamoin, C. Rey, Parameter identification and model updating in the context of nonlinear mechanical behaviors using a unified formulation of the modified constitutive relation error concept, Comput. Methods Appl. Mech. Engrg. 345 (2019) 1094–1113.
[38] H. Montazerian, A. Rashidi, A.S. Milani, M. Hoorfar, Integrated sensors in advanced composites: A critical review, Crit. Rev. Solid State Mater. Sci. 45 (3) (2020) 187–238.
[39] P. Virtanen, R. Gommers, T.E. Oliphant, M. Haberland, T. Reddy, D. Cournapeau, E. Burovski, P. Peterson, W. Weckesser, J. Bright, S.J. van der Walt, M. Brett, J. Wilson, K.J. Millman, N. Mayorov, A.R.J. Nelson, E. Jones, R. Kern, E. Larson, C.J. Carey, İ. Polat, Y. Feng, E.W. Moore, J. VanderPlas, D. Laxalde, J. Perktold, R. Cimrman, I. Henriksen, E.A. Quintero, C.R. Harris, A.M. Archibald, A.H. Ribeiro, F. Pedregosa, P. van Mulbregt, SciPy 1.0 Contributors, SciPy 1.0: Fundamental algorithms for scientific computing in python, Nature Methods 17 (2020) 261–272, http://dx.doi.org/10.1038/s41592-019-0686-2.